A Tunable Pulmonary Organoid Model Demonstrates Compositionally Driven Epithelial Plasticity and Immune Polarization

Sophie E. Edelstein[1,2], Satoshi Mizoguchi[1,2], Maria Tomàs Gracia[1,2,3], Nuoya Wang[1,2], Vi Lee[1,2], Hahram Kim[1,2], Connor Haynes[3], Colten Danelski[4], Tomoshi Tsuchiya[5], Maor Sauler[6,7], Micha Sam Brickman Raredon[1,2,8,7,*]

[1] Department of Anesthesiology, Yale School of Medicine, New Haven, CT 06520, USA
[2] Vascular Biology and Therapeutics Program, Yale School of Medicine, New Haven, CT 06520, USA
[3] Medical Student Training Program, Yale School of Medicine, New Haven, CT 06520, USA
[4] Department of Biomedical Engineering, Yale University, New Haven, CT 06511, USA
[5] Department of Thoracic Surgery, University of Toyama, Toyama, 9300194, Japan
[6] Department of Pulmonary, Critical Care and Sleep Medicine, Yale School of Medicine, New Haven, CT 06520, USA
[7] Center for Pulmonary Injury, Inflammation, Repair and Therapeutics (CPIRT), Yale School of Medicine, New Haven, CT 06520, USA
[8] Program in Translational Biomedicine (PTB), Yale School of Medicine, New Haven, CT 06520, USA
* Correspondence to michasam.raredon@yale.edu

Summary/Abstract

Aberrant epithelial regeneration and immune remodeling are hallmarks of chronic lung diseases such as idiopathic pulmonary fibrosis (IPF), COPD, and post-viral syndromes. Yet how cellular context shapes these trajectories remains unresolved. We present a tunable, primary rat-derived lung organoid model that systematically varies immune, epithelial, and mesenchymal inputs to reveal how composition alone dictates epithelial plasticity and macrophage polarization. Across conditions, we observed the spontaneous emergence of disease-relevant transitional cell states—including Sox9+ stressed progenitors, RAS/AT0-like intermediates, and hillock-like cells—alongside distinct macrophage activation profiles. In mesenchyme-rich contexts, epithelial–immune–mesenchymal crosstalk appeared to reinforce inflammatory signaling and stabilize transitional persistence, while immune-dominant inputs favored ATI-like repair and squamous remodeling. Notably, hillock-like cells displayed context-specific polarization and expressed immune-regulatory genes, suggesting a role as epithelial orchestrators that help calibrate inflammatory response during regeneration. Connectomic analysis revealed that regenerative outcomes were associated with dynamic multicellular signaling networks that integrate stress sensing, immune coordination, and epithelial fate. This platform provides a tractable system for modeling context-specific repair and regenerative mechanisms and could inform therapeutic strategies aimed at redirecting epithelial fate in chronic lung disease.

Introduction

Epithelial plasticity is a defining feature of lung homeostasis, injury repair, and disease progression (Beppu et al., 2023). Lung regeneration depends on dynamic interactions among epithelial, immune, and mesenchymal lineages. During injury and repair, epithelial cells transition through distinct phenotypical and transcriptomic states in response to microenvironmental cues, exemplified by transitional populations such as hillock, activated respiratory airway secretory (aRAS), alveolar type 0 (AT0) and damage associated transient progenitor (DATP) cells (Lin et al., 2024; Kadur Lakshminarasimha Murthy et al., 2022; Basil et al., 2021; Tata & Rajagopal, 2017; Choi et al., 2020). Such transitions are shaped by crosstalk with mesenchymal and immune cells, which influence key outcomes such as alveolar re-epithelialization, matrix remodeling, and the resolution or persistence of inflammation that ultimately determine whether tissues regenerate successfully or deviate toward pathologic states.

Traditional 2D epithelial culture systems fail to recapitulate native tissue architecture and lack immune and mesenchymal components, which are essential for regulating epithelial steady state and fate (Barnes et al., 2023; Jones et al., 2023). Conversely, while in vivo animal models provide a physiologically relevant context, they do not allow for systematic dissection of how specific cellular lineages and the specific ratios of these lineages shape epithelial behavior under controlled conditions (Murrow et al., 2017).

Mesenchymal populations, in particular, are critical regulators of both epithelial and immune cell behavior (Zepp et al., 2017; Ghonim et al., 2023). Epithelial–mesenchymal crosstalk plays a well-established role in lung development and alveolar differentiation, regulating epithelial proliferation and fate via WNT and BMP signaling (Goltsis et al., 2024; Xu et al., 2011; Frum et al., 2023). In parallel, mesenchymal cells influence immune cell polarization and cytokine production, modulating inflammatory milieu and repair outcomes (Morrison et al., 2017; Mo et al., 2022). These regulatory axes converge in injury contexts, where signals such as IL-33, IL-1β, and TNF-α help coordinate epithelial and immune responses during tissue remodeling (de Kleer et al., 2016; Wang et al., 2024; Katsura et al., 2019). Despite this, the precise ways in which mesenchymal presence or absence governs epithelial–immune coordination in the rat remain difficult to isolate in vivo.

Pulmonary organoid models offer a promising approach to study epithelial plasticity and multicellular dynamics in defined systems (Nikolic & Rawlins, 2017). However, many rely on genetic modifications, exogenous injury cues, or predefined differentiation protocols to drive epithelial transitions (Leko et al., 2023; Sachs et al., 2019; Abo et al., 2022). Here, we present a lung organoid model that leverages primary lung-derived populations to explore both epithelial plasticity and immune cell behavior—particularly macrophage polarization—without externally imposed injury or lineage-specific cues.

To directly explore how native cellular composition influences epithelial plasticity under uniform culture conditions, we developed a tunable organoid system using primary rat-derived lung populations. Our system begins with two distinct inputs from the same

lung: (1) a pulmonary dissociation (PD) fraction, generated through enzymatic digestion of whole lung tissue, yielding a heterogeneous mix of epithelial, mesenchymal, endothelial, and immune cells; and (2) a bronchoalveolar lavage (BAL) fraction, obtained by perfusing the lung with cold saline to collect non-adherent immune cells from airway surfaces. These inputs were combined in controlled ratios to generate three organoid conditions: 100% PD (PD_3D), 100% BAL (BAL_3D), or a 1:1 mix (Mixed_3D).

Reparative-like conditions emerged spontaneously across all cultures, consistent with prior observations that engineered tissues often undergo stress-associated remodeling when removed from native physiological regulation (Zhang et al., 2024; Liu et al., 2015; Patel et al., 2018). Although all organoids were maintained under identical media, matrix, and environmental parameters—including supportive growth factors and a 5% CO_2 atmosphere (Nichane et al., 2017)—distinct epithelial and immune states reproducibly emerged across PD_3D, BAL_3D, and Mixed_3D conditions. These included injury-associated epithelial features such as hillock-like clusters and activated RAS cells, as well as condition-specific macrophage polarization patterns (Basil et al., 2022; Lim et al., 2024). These outcomes were not driven by external perturbations but instead correlated with differences in starting cellular composition. While our system does not model injury directly, organoid cultures inherently recapitulate certain stress-like features—such as local hypoxia, nutrient diffusion limitations, and absence of physiological feedback—that may sensitize cells toward transitional or reparative states (Nwokoye & Abilez, 2024; Corro et al., 2020).

Within this shared, stress-permissive environment, our findings suggest that initial cellular makeup shapes how multicellular interactions unfold, offering a biologically grounded platform to study how lung tissues navigate between homeostatic, reparative, and pathological states. Across all three organoid conditions, we observed reproducible emergence of transitional epithelial states and macrophage polarization patterns that are not externally imposed but arise from differences in starting composition. This may suggest that cellular ratios at the onset of culture can direct divergent regenerative trajectories, with immune enrichment favoring certain reparative or inflammatory fates and mesenchymal presence modulating epithelial state transitions. By enabling systematic variation in epithelial, immune, and mesenchymal inputs, our model provides an experimental framework to interrogate how compositional tuning influences developmental and injury-associated programs—a principle with broad implications for regenerative biology and therapeutic modulation of lung repair.

Results

A compositionally tunable lung organoid system enables controlled investigation of epithelial and immune state emergence

We began our study with two biologically grounded inputs isolated from the native rat lung—an organ whose developmental trajectory, anatomical architecture, and cellular composition closely mirror those of the human lung, making it a robust model for studying epithelial dynamics in health and disease (Warburton et al., 2000; O'Reilly & Thébaud, 2014; Burri, 1974; Nardell & Brody, 1982). Our two starting populations were: (1) a pulmonary dissociation (PD) fraction, generated through enzymatic digestion of whole lung tissue, which yielded a heterogeneous mixture of epithelial, mesenchymal, endothelial, and immune cells; and (2) a bronchoalveolar lavage (BAL) fraction, obtained by saline perfusion, which was enriched for non-adherent immune cells—including macrophages, neutrophils, B cells, and T cells—and contained a small subset of rare airway epithelial progenitors (**Fig. 1a**).

scRNA-seq of these starting populations confirmed that PD (n = 3 - 9,730 cells) contained a diverse set of epithelial subsets—namely alveolar type 1 (*Pdpn*$^+$/*Ager*$^+$) (AT1), alveolar type 2 (*Sftpc*$^+$/*Napsa*$^+$/*Lamp3*$^+$) (AT2), basal (Krt5$^+$/*Tp63*$^+$), secretory (Scgb3a1$^+$/*Scgb3a2*$^+$), ciliated (*Ccdc153*$^+$/*Pifo*$^+$), and tuft cells (*Dclk1*$^+$/*Trpm5*$^+$)—as well as mural (*Acta2*$^+$/*Actc1*$^+$) mesenchyme, *Msln*$^+$ mesothelium, arterial (*Gja5*$^+$/*Dll4*$^+$), venous (*Slc6a2*$^+$/*Tmem252*$^+$), and capillary (*Wif1*$^+$/*Aplnr*$^+$) endothelial cells, and a variety of innate and adaptive immune components (**Fig. 1b–f; Supplemental Fig. 2d–x**). In contrast, BAL (n = 32,009 cells) was largely restricted to myeloid populations (*Pparg*$^+$/*Prodh2*$^+$) and lymphoid populations (*Cd3e*$^+$/*Cd79b*$^+$), with only a small population of epithelial cells (**Fig. 1b–d; Supplemental Fig. 1a-d**).

To generate three distinct starting populations, PD and BAL isolates were used individually or in combination: PD_3D (100% PD), BAL_3D (100% BAL), and Mixed_3D (a 50:50 mix of BAL and PD) (**Fig. 1a**). All cell suspension mixtures were resuspended in Matrigel and maintained in identical cell culture media supplemented with broadly supportive growth factors and small molecules, including Fgf10, Egf, and inhibitors of TGFβ and GSK3 signaling and a 5% CO_2, 37°C environment (Nichane et al., 2017) (**Fig. 1a**).

Over the 10-day culture period, organoids formed and expanded in all conditions, but each exhibited distinct growth kinetics and morphologies (**Fig. 1g–h**). PD_3D cultures demonstrated rapid expansion by day 3, both in organoid number and surface area. Early branching and increased structural complexity were evident. As the culture progressed, PD_3D organoids enlarged to the point of physical contact, forming a dense, interconnected, web-like structure. Notably, despite continued increases in organoid area (**Fig. 1h, Fig. 2a**), the number of discrete organoids declined over time (**Fig. 1g**), suggesting that individual organoids may have fused as they expanded. Many of the largest organoids appeared enriched for ATI-like cells—the thin, flattened

epithelial cells critical for gas exchange within the body—based on their morphology (**Fig. 2k, n**).

Mixed_3D cultures exhibited a phenotype intermediate between PD_3D and BAL_3D, both in growth and architecture. Organoid counts were higher than in BAL_3D, but lower than in PD_3D (**Fig. 1g**), and organoid areas increased steadily over time, although they remained smaller on average than those in BAL_3D by day 10 (**Fig. 1h**). Structurally, Mixed_3D organoids displayed a blend of compact and branching morphologies, with occasional early complexity reminiscent of PD_3D, yet without the extensive fusion or web-like architecture observed in PD_3D by day 10 **(Fig. 2h–j)**

In contrast, BAL_3D cultures exhibited slower kinetics and generated fewer organoids overall, yet the structures that did form were consistently larger than those in other conditions (**Fig. 2h**). BAL_3D uniquely gave rise to a subset of complex, floret-like organoids with branching extensions that resembled lung-budding architecture (**Fig. 2e–g**)—a morphology not observed in PD_3D. These structures suggested the emergence of specialized epithelial subtypes and indicate distinct differentiation trajectories within BAL-derived progenitor populations.

To understand how these morphologies related to underlying cell fate outcomes, we performed scRNA-seq on each system (condition) on Day 10 (*see Methods*). Distinct lineage outputs were evident across conditions (**Fig. 2x–z**). PD_3D and Mixed_3D retained epithelial, immune, and mesenchymal populations. In contrast, BAL_3D lacked mesenchymal cells altogether, as did the starting population on Day 0. Endothelial populations, present in PD and Mixed_3D at Day 0, were largely absent by Day 10 across all conditions, consistent with limited endothelial survival in an epithelial-enrichment culture medium that lacks growth factors to support endothelial growth, such as VEGF and FGF2 (Seo et al., 2016; Worsdorfer et al., 2019) (**Fig. 1f**). *Pdgfrb*$^{+}$ pericytes and *Rspo3*$^{+}$ fibroblasts were selectively maintained in Mixed_3D and PD_3D, in varying proportions (**Fig. 2dd**).

Interestingly, BAL_3D—despite lacking mesenchymal cells—contained the second largest number of ATI-like cells (BAL_3D: 5.16 ± 3.88%; Mixed_3D: 5.60 ± 1.70%; PD_3D: 2.68 ± 0.54%) (**Fig. 2bb**). This observation contrasts with expectations based on prior reports that mesenchymal derived signaling pathways (including Wnt, BMP, FGF, TGFβ, and YAP/TAZ) support alveolar epithelial differentiation (Zhao et al., 2013; Jeon et al., 2022; Nabhan et al., 2022). While our data do not exclude a supportive role for mesenchyme, they suggest that other cues—such as immune-derived signals—may coincide with increased ATI differentiation in this system. Specifically, we detected high expression of insulin-like growth factor I (*Igf1*) and interleukin-1 beta (*IL-1β*) in immune populations across all three conditions (**Supplemental Fig. 8c–d**). This finding is consistent with prior work showing that *Igf1* can promote ATII-to-ATI differentiation through activation of *Wnt5a* signaling (Ghosh et al., 2013). Similarly, *Il1b* has been shown to prime a subset of ATII cells for alveolar regeneration by inducing their transition into DATPs through a HIF1α-mediated glycolysis pathway—a critical step

required for subsequent differentiation into mature ATI cells (Choi et al., 2020). Our results raise the possibility that in the absence of mesenchymal cells, immune-derived factors such as *Igf1* and *Il1b* may play a compensatory or prominent role in shaping ATI-like differentiation dynamics.

Epithelial composition varied by input. PD_3D cultures generated a full spectrum of epithelial states, including ATII-like, ATI-like, basal, secretory, and RAS-like subtypes. BAL_3D cultures, despite beginning with only 4.8 ± 7.3% epithelial cells, gave rise to a comparable range of epithelial types (**Fig. 1c; Fig. 2bb**). Basal cells were more prominent in BAL_3D (9.33%) compared to PD_3D (7.1%) and Mixed_3D (5.9%). RAS-like and secretory populations emerged across all three conditions, consistent with their roles in transitional remodeling. Mixed_3D cultures exhibited epithelial features seen in both PD_3D and BAL_3D, along with distinct combinations—such as ATI-like cell representation comparable to BAL_3D (5.60% vs. 5.16%, respectively), and the presence of pericytes also seen in PD_3D and Mixed_3D (**Fig. 2bb, dd**). These findings underscore that initial cellular composition influences epithelial diversity not by generating unique lineages per condition, but by modulating the proportional balance and co-occurrence of shared cell states.

Together, these data established our organoid platform as a compositionally tunable and biologically grounded system in which divergent cell states emerge from distinct starting populations under identical environmental conditions. The robust expansion of epithelial cells from BAL despite minimal epithelial input, the differential survival of mesenchymal and endothelial populations, and the emergence of distinct tissue morphologies and lineage distributions all underscore the capacity of this system to model how initial cellular context shapes downstream epithelial and immune organization and differentiation.

Emergence of Polarized Hillock Cells Reveals Condition-Specific Epithelial Trajectories

In characterizing the epithelial landscape across conditions at day 10, we identified a prominent population of *Krt13*$^{+}$/*Sprr1a*$^{+}$ cells co-expressing either *Krt5 or Adm*, suggestive of hillock-like domains. These populations emerged spontaneously in our culture systems without exogenous injury cues, highlighting their intrinsic responsiveness to environmental remodeling. To confirm the relevance of these findings, we examined the native rat trachea—where hillock cells have not previously been described—and identified organized clusters of *Krt13*$^{+}$ cells within the basal epithelium (**Fig. 3a–c**). These structures recapitulated the hallmark architecture of hillock domains observed in mouse and human airways: a stratified layer of Krt13^{+} squamous cells positioned above an underlying *Krt5*$^{+}$ basal stem cell pool (Montoro et al., 2018; Lin et al., 2024). We further validated their emergence in vitro by staining day 10 organoids, which contained discrete foci of similarly layered *Krt13*$^{+}$/*Krt14*$^{+}$ populations (**Fig. 3j-o**). *Sprr1a*, a member of the small proline-rich (*Sprr*) protein family, has been implicated in terminal squamous differentiation and the formation of the cornified envelope in keratinocytes (Zimmerman et al., 2004; Zheng et al., 2008; Strunz

et al., 2019). Its co-expression with *Krt13* in this context supports a model in which these epithelial populations are engaging in a mature squamous differentiation program.

Single-cell RNA sequencing data of our organoid models revealed that these *Krt13*$^{+}$ cells clustered distinctly within the proximal epithelial subset (**Fig. 3d**) and could be further subdivided into two transcriptionally polarized populations: hillock basal (*Krt13*$^{+}$*/Krt5*$^{+}$*/Sprr1a*$^{+}$) and hillock luminal (*Krt13*$^{+}$*/Sprr1a*$^{+}$*/Krt5*$^{-}$), in line with previously characterized hillock subtypes in murine and human lung (Lin et al., 2024; Montoro et al., 2018; Otto et al., 2025). Notably, we observed condition-specific polarization in the proportions of each subtype: BAL_3D cultures, derived from an immune-dominant and mesenchymal-poor starting population, were enriched for hillock basal cells; in contrast, Mixed_3D and PD_3D conditions, which began with more compositionally diverse cell populations, favored the hillock luminal phenotype (**Fig. 3d**). The immune-rich context of BAL_3D supports a basal-skewed hillock state, while epithelial–mesenchymal heterogeneity supports luminal differentiation (**Fig. 3e**). As the starting epithelial compartment in BAL largely recapitulates that of PD, albeit at lower abundance (**Supplemental Fig. 1b, d; Supplemental Fig. 2a, d**), these findings point to microenvironmental cues—rather than epithelial-intrinsic differences—as key drivers of hillock subtype polarization.

To investigate the differentiation dynamics of these populations, we applied Slingshot pseudotime analysis, which revealed a clear trajectory progressing from proximal cycling epithelial cells through basal-like (*Krt5*$^{+}$*/Sprr1a*$^{+}$*/Krt13*$^{-}$) and basal hillock-like (*Krt5*$^{+}$*/Krt13*$^{+}$), ultimately terminating in hillock luminal (**Fig. 3f–h**). This trajectory demonstrates that the more squamous, hillock luminal cells may arise from hillock basal cells, representing a more differentiated or specialized form of the hillock lineage, as suggested by earlier findings (Lim et al., 2024).

In parallel with this trajectory, we found that hillock luminal cells also upregulate a distinct suite of immune-associated genes, including *Slpi, Mal, S100a7, Il1a, and S100a8* (**Fig. 3e**). The aforementioned genes are classically linked to antimicrobial defense, damage sensing, and inflammatory signaling at barrier surfaces. These functions are increasingly attributed to epithelial cells in injury and regenerative contexts (Hewitt & Lloyd, 2021).

Slpi, an epithelial-derived serine protease inhibitor, protects barrier integrity by neutralizing neutrophil elastase and modulating cytokine release (Camper et al., 2015). *Il1a*, a pro-inflammatory cytokine, is rapidly produced by epithelial cells in response to stress, necrosis, or damage, where it acts as an alarmin to recruit and activate immune cells (Suwara et al., 2014). In addition, *Mal*, a proteolipid involved in mediating apical sorting among polarized epithelial cells, ensuring the proper delivery of proteins to the apical membrane, as well as facilitating Lck trafficking in T cells for TCR-immune activation (Cao et al., 2012; Anton et al., 2008). *S100a7* (psoriasin) and *S100a8* are calcium-binding proteins released by squamous epithelial cells under inflammatory conditions, where they promote neutrophil chemotaxis and amplify innate immune

signaling (Liu et al., 2022; Wang et al., 2022). The expression of such genes by luminal hillock suggests that these polarized epithelial cells may uniquely contribute to epithelial–immune communication, serving not merely as transitional intermediates but as immunomodulatory effectors within the remodeling airway epithelium.

To further dissect the functional specialization within the hillock population, we compared hillock luminal cells to hillock basal cells using MSigDB Hallmark pathway enrichment (Liberzon et al., 2015). This analysis revealed that luminal cells are significantly enriched for pathways associated with inflammatory signaling, immune communication, and stress adaptation, including TNFα signaling via NF-κB, IL2/STAT5 signaling, complement, TGF-β signaling, and hypoxia (**Fig. 3i**). In contrast, hillock basal cells were enriched for proliferative programs such as MYC targets, E2F targets, and G2M checkpoint, suggesting a more canonical basal epithelial state engaged in cell cycle regulation (**Fig. 3i**) (Dong et al., 2014).

The signaling profile of hillock luminal cells—marked by elevated cytokine and alarmin expression alongside inflammatory pathway activation—supports a model in which these cells represent a regulatory epithelial state. Drawing on the framework proposed by Medzhitov (2021), this pattern is consistent with an epithelial response to loss of regulatory control, in which classical homeostatic mechanisms are insufficient, and inflammation is repurposed to enforce system-level coordination.

To corroborate these transcriptional and pathway-based findings, we examined the spatial organization of hillock populations using multiplex immunofluorescence staining of day 10 organoids. Across BAL_3D, PD_3D, and Mixed_3D conditions, we observed distinct patterns of *Krt13*$^{+}$ cell localization along the apical surface of epithelial organoids (**Fig. 3j–o**). In BAL_3D cultures, *Krt13*$^{+}$ cells co-expressed *Krt14* and assembled into a rigid, stratified structure that encompassed the entire organoid surface, forming a multilayered squamous barrier that dominated the epithelial architecture (**Fig 3l**). In contrast, organoids from PD_3D and Mixed_3D conditions exhibited *Krt13*$^{+}$/*Krt14*$^{-}$ luminal cells with a flattened, apically aligned morphology, more sparsely distributed along the epithelial surface (**Fig. 3j, k, n**). Importantly, in these latter conditions, a subset of hillock luminal cells also co-expressed *Scgb1a1*, consistent with their transcriptional signature and supporting a model in which *Krt13*$^{+}$/*Scgb1a1*$^{+}$ cells define a distinct, differentiated luminal hillock state (**Fig. 3j, n**).

Taken together, these results reveal that hillock-like cells emerge spontaneously from native lung-derived within organoid cultures and adopt distinct basal or luminal identities depending on the starting cellular context. Their spatial organization, differentiation trajectory, and expression of immune-associated genes suggest a dual role in epithelial remodeling and immune coordination. As such, hillock cells in our system serve not only as a marker of epithelial plasticity, but as a window into the multicellular dynamics that shape airway regeneration and inflammation.

Culture Composition Dictates Divergent Macrophage Activation Programs

Across all three engineered conditions, we observed a significant loss of immune populations over the 10-day culture period. Despite this overall depletion, a subset of macrophages consistently persisted, particularly in BAL_3D and Mixed_3D—the two conditions that began with higher immune representation at day 0 (**Fig. 4d**). In contrast, macrophages were rare (0.81 ± 1.26%, n=3) in PD_3D by day 10, consistent with the lower abundance of immune cells in the initial PD input (**Fig. 4d)**. Macrophages were not embedded within the organoid structures themselves nor enclosed within luminal spaces but instead remained dispersed throughout the extracellular matrix. These solitary, matrix-associated macrophages were spatially separated from epithelial cells, suggesting that their influence was mediated through paracrine signaling rather than direct cell–cell contact (**Fig. 4e**).

To further characterize macrophage heterogeneity, we subclustered the immune compartment and identified three transcriptionally distinct macrophage clusters (**Fig. 4a**). To investigate whether the macrophages that persisted across conditions adopted distinct activation states, we performed differential gene expression analysis on this subset, comparing cluster 0 (enriched in BAL_3D) to clusters 1 and 2 (enriched in Mixed_3D and PD_3D). The resulting transcriptional programs did not fully align with classical M1/M2 macrophage paradigms but instead resembled anti-inflammatory-like and pro-inflammatory-like states (**Fig. 4a–b**) (Guan et al., 2023).

Anti-inflammatory-like macrophages, which predominated in BAL_3D, expressed genes associated with immune regulation and resolution, including *Pparg, Cd84, Cadm1, and Cela1* (**Fig. 4g**). *Pparg*, a nuclear receptor and transcriptional regulator of alternative macrophage activation, is known to suppress inflammatory gene programs—often through inhibition of canonical NF-κB signaling—and promote lipid handling, tissue repair, and immunoregulation in the lung (Nolte et al., 1998; Neri et al., 2011). *Cd84*, a SLAM family receptor broadly expressed in leukocytes, has been shown to modulate macrophage activation downstream of *Tlr4* (Sintes et al., 2010). While *Cd84* has been shown to enhance MAPK and NF-κB signaling in response to LPS, recent evidence suggests that NF-κB is not uniformly pro-inflammatory; in specific contexts, it can repress inflammatory mediators and promote resolution by upregulating *Il10* and inducing apoptosis in activated leukocytes (Sintes et al., 2010; Radomir et al., 2021). Thus, *Cd84* expression may reflect a tuning mechanism—enabling macrophages to remain responsive while mitigating excessive inflammation. *Cadm1*, an adhesion molecule linked to tissue-resident macrophages and epithelial interaction, may further support macrophage localization and immune-epithelial coordination (Ramos et al., 2022). Finally, *Cela1*, traditionally associated with epithelial cells during postnatal alveolar remodeling, has also been observed in macrophages during lung development—where it contributes to elastase activity and extracellular matrix turnover (Joshi et al., 2018).

Anti-inflammatory-like macrophages, which predominated in BAL_3D, expressed a coordinated program of immune regulatory and tissue-adaptive genes, including *Pparg*, *Cd84*, *Cadm1*, and *Cela1* (**Fig. 4g**). *Pparg*, a nuclear receptor known to repress inflammatory gene expression, likely acts upstream to promote alternative activation and lipid handling (Nolte et al., 1998; Neri et al., 2011). *Cd84*, a SLAM family receptor, may reinforce this anti-inflammatory response by modulating NF-κB signaling during inflammation (Sintes et al., 2010). *Cadm1* and *Cela1* further point to tissue adaptation: *Cadm1* has been implicated in macrophage-epithelial interactions, while *Cela1*, although canonically epithelial, contributes to extracellular matrix remodeling and has been detected in macrophages during lung development (Ramos et al., 2022; Joshi et al., 2018). Together, these features suggest that in the absence of mesenchymal signals, macrophages may adopt a tissue-adaptive phenotype that supports remodeling and epithelial barrier stabilization.

Pro-inflammatory macrophages, enriched in Mixed_3D, showed upregulation of genes associated with acute inflammatory signaling, leukocyte recruitment, and matrix remodeling (**Fig. 4g**). These included *Cxcl1*, *Cxcl2*, and *Cxcl3*, potent neutrophil chemoattractants that signal through *Cxcr2* and amplify tissue inflammation (Zhou et al., 2023). Concurrent expression of *Il1a* and *Nos2* reflects classic M1-like features: Il1a being a master cytokine for amplifying local inflammation, and *Nos2* catalyzing nitric oxide production, contributing to microbicidal activity and tissue damage (Raja et al., 2024; Palmieri et al., 2020). In line with this activated state, a subset of these macrophages also exhibited G2M and S phase signatures, suggesting ongoing cell cycle progression—a feature commonly associated with activation-induced expansion in inflammatory macrophage populations (**Fig. 4c**) (Micochova et al., 2024). Notably, this pro-inflammatory program emerged predominantly in conditions that retained mesenchymal populations (Mixed_3D and, to a lesser extent, PD_3D), while it was absent in BAL_3D, which lacked mesenchyme from the start. This suggests that mesenchymal-derived cues may drive macrophage inflammatory polarization under otherwise shared culture conditions.

To further characterize the relationship between macrophage states, we performed pseudotime analysis across the immune subset (**Fig. 4f**). This revealed a continuous trajectory spanning from the anti-inflammatory cluster to the pro-inflammatory cluster, suggesting these populations may not represent fixed or terminal identities, but instead exist along an activation spectrum. Enrichment along this spectrum appeared tunable by microenvironmental composition, with early pseudotime points disproportionately represented in mesenchyme-containing conditions.

Sox9^{+} Transitional States and RAS-Like Cells Define Alternative Regenerative Programs

Injury-associated epithelial progenitor states have emerged as critical regulators of distal lung regeneration—and, when dysregulated, key contributors to disease (Alysandratos et al., 2021). In clinical contexts such as idiopathic pulmonary fibrosis

(IPF) and chronic obstructive pulmonary disease (COPD), epithelial remodeling is frequently marked by the expansion of transitional populations, including *Sox9*$^{+}$ progenitor-like cells and secretory-biased intermediates, which deviate from normal alveolar differentiation trajectories and contribute to distal repair (Cai et al., 2024; Basil et al., 2022). Although *Sox9*$^{+}$ progenitor cells are present at low levels in the healthy lung, their expansion is associated with alveolar injury, aberrant regeneration, and impaired lineage resolution (Sun et al., 2022; Cai et al., 2024).

Among the transitional populations increasingly recognized in human distal lung biology are respiratory airway secretory (RAS) cells and alveolar type 0 (AT0) cells—both of which exhibit hybrid phenotypes that bridge canonical secretory and alveolar identities. RAS cells, first described by Basil et al. (2022), are a distinct secretory population found within ferret and human respiratory bronchioles, defined by high expression of *SCGB3A2* and *SCGB1A1.* When activated in injury contexts, these cells exhibit additional transcriptional proximity to AT2 cells (*SFTPC*). Functionally, RAS cells may act as progenitors that give rise to alveolar epithelium in organoid models and are transcriptionally altered in smokers and individuals with COPD, suggesting a role in disease-associated remodeling.

AT0 cells, described by Murthy et al. (2022), represent a bipotent transitional state observed during regeneration following alveolar injury. These cells co-express *SFTPB*, *SCGB1A1*, and *SCGB3A2*, and occupy a developmental trajectory capable of differentiating into both AT1, AT2, and secretory cell types. AT0s emerge in the respiratory bronchiole–alveolar interface, are conserved across species, and are particularly prominent in models of lung repair. Notably, they are transcriptionally and spatially distinct from classical AT2 cells and canonical secretory lineages, localizing to a niche not typically populated by either cell type and associated with sites of active epithelial remodeling.

Prior to the identification of these transitional intermediates, the bronchioalveolar stem cell (BASC) was considered the principal epithelial progenitor population in the distal lung. First characterized in murine models, BASCs reside at the bronchioalveolar duct junction (BADJ) and are uniquely marked by co-expression of *Scgb1a1* and *Sftpc*, reflecting their potential to give rise to both bronchiolar (secretory) and alveolar (AT2) lineages (Kim et al., 2005). These cells are resistant to epithelial injury, expand following damage, and display both self-renewal and multilineage differentiation in vitro and in vivo (Kim et al., 2005; Salwig et al., 2019). As such, BASCs are often regarded as a bipotent epithelial progenitor that maintains epithelial homeostasis in the distal lung. However, their orthologues in the human lung remains unclear, and mounting evidence suggests that additional injury-associated progenitor states—such as RAS and AT0 cells—may functionally equivalent to or even supersede BASCs in settings of regeneration and disease (Martins et al., 2024). This evolving understanding underscores the diversity of regenerative strategies employed by the distal epithelium, particularly under conditions of stress or injury.

In support of the findings reported by others, we identified rare *Sox9*$^{+}$ cells localized near the bronchoalveolar junction (BADJ) in native adult rat lung, occasionally co-expressing *Scgb1a1*, consistent with previous descriptions of bipotent progenitor populations (**Fig. 5a**). Similarly, *Scgb3a2*$^{+}$ secretory cells were enriched in conducting airway epithelium (**Fig. 5b**), reflecting spatial patterns that parallel those observed in human and ferret respiratory bronchioles.

In our organoid models, a progenitor-like population resembling BASCs—marked by *Scgb1a1/Sftpc/Sox9* expression—expanded across all three culture conditions (**Fig. 5d, h-j**). However, these cells also exhibited a transcriptional shift not characteristic of canonical BASCs, whereby they adopted a stress-associated gene program that included *Cox4i2*, *Ptges*, and *Stc1* after ten days in culture (**Fig. 5e**). This co-expression of epithelial progenitor and stress markers suggests that these *Sox9*+ transitional cells may represent an injury-responsive intermediate state, shaped by both intrinsic plasticity and extrinsic cues within the controlled culture environment (**Fig. 5c, e**).

The co-expression of *Cox4i2*, a nuclear subunit of cytochrome c oxidase (complex IV of the electron transport chain), and *Sox9*, a marker of alveolar-regenerating adult progenitors as well as distal tip progenitors in the fetal lung, suggests a unique phenotype in this population. These stressed progenitors may have initially expanded to facilitate repair but later required a metabolic shift to support survival. The upregulation of Cox4i2 may reflect this adaptation, enabling more efficient ATP generation within the specific constraints of the organoid milieu (Aras et al., 2013; Rockich et al., 2013).

In parallel, the upregulation of *Ptges* and *Stc1* may further indicate that such stressed *Sox9*$^{+}$ progenitors are not only expanding to serve as a reserve pool of multipotent progenitors but actively contributing to the modulating repair of the system. *Ptges*, involved in PGE2 synthesis, has strong links to modulating inflammation while *Stc1*, a secreted glycoprotein hormone, has been shown to activate anti-apoptotic signaling in injury contexts (Block et al., 2009; Liu et al., 2012).

RAS-like epithelial states were detected across all three conditions, marked by co-expression of *Scgb1a1*, *Scgb3a2*, and *Sftpc*. These cells were most abundant in PD_3D and Mixed_3D, where mesenchymal populations were retained, as demonstrated by both RAS signature scoring and individual gene expression (**Fig. 5f-g**, **Supplemental Fig. 7d, h, l**). Canonical secretory cells (*Scgb1a1*$^{+}$/*Scgb3a2*$^{+}$/*Sftpc*$^{-}$) were also present across conditions but did not exhibit alveolar features. Notably, the RAS-like state was not exclusive to any single input, nor did it require exogenous injury to emerge. Instead, its relative abundance appeared to be shaped by the presence or absence of mesenchymal components, suggesting that epithelial–mesenchymal–immune interactions influence the balance of transitional and differentiated epithelial states under homeostatic culture conditions.

Intra-Lineage Signaling Coordinates Epithelial, Immune, and Mesenchymal Regenerative Response

Understanding how diverse cellular inputs shape epithelial and immune behavior requires not only classifying cell states but also mapping the signaling cues that guide them. While our earlier analyses revealed condition-specific emergence of distinct macrophage and hillock phenotypes, the mechanisms coordinating these shifts remained unclear. Given the established role of mesenchymal cells in producing paracrine factors that influence both epithelial differentiation and immune polarization, we hypothesized that variation in mesenchymal presence could modulate these outcomes through context-specific signaling programs (Enomoto et al., 2023; Manneken & Currie, 2023; Negretti et al., 2025).

To investigate this, we applied NICHES (*Niche Interactions and Communication Heterogeneity in Extracellular Signaling*), a framework that quantifies ligand-receptor signaling potential between individual cells based on single-cell transcriptomic data (Raredon et al., 2023). Unlike methods that aggregate interactions at the cluster level, NICHES evaluates pairwise signaling events between cells, allowing us to resolve how communication between epithelial, mesenchymal, and immune compartments varies across engineered conditions (**Fig. 6a**). This approach enabled identification of signaling axes enriched in mesenchyme-rich (Mixed_3D) versus mesenchyme-poor (BAL_3D) contexts, including those involving pro-regenerative, pro-inflammatory, and immunomodulatory ligands (**Fig. 6b**).

To simplify interpretation of cross-lineage signaling, we grouped hillock and macrophage subsets into unified epithelial and immune populations. Unsupervised clustering of the NICHES CellToCell matrix grouped ligand-receptor interactions into discrete signaling modules, each enriched for specific sender–receiver pairings. These modules revealed dominant communication routes—such as epithelial-to-immune or immune-to-mesenchymal—that varied across conditions, highlighting how lineage-specific signaling shifts in different cellular contexts.

Given the emergence of distinct macrophage and epithelial phenotypes across conditions, we hypothesized that these context-specific cell states were driven by differential expression of ligand–receptor pairs mediating cross-compartmental signaling. To test this, we cross-referenced known ligand–receptor interactions from the FANTOM5 database with genes expressed in our dataset to assemble high-confidence sender–receiver pairs (Ramilowski et al., 2015). We then performed differential expression analysis within each cell subset ($\log_2$ fold-change > 0.25, expressed in ≥25% of cells) and calculated a power metric (expression ratio × avg. $\log_2$FC) to prioritize signaling interactions that were both differentially expressed and population-specific.

Confirming our hypothesis, this analysis revealed a prominent signaling axis connecting hillock epithelial cells and macrophages. Ligands such as *Serpina1, Cd24, Il1rn,* and *Il1a* were co-expressed in both populations and targeted receptors on mesenchymal

and immune cells (**Fig. 6c-d**). For instance, *Serpina1—Lrp1* and *Cd24—Selp* suggest potential roles for hillock cells in regulating macrophage adhesion and activation (**Fig. 6e**) (Morrow et al., 2024; Garcia-Arcos, 2022). In parallel, *Il1rn—Il1r1, Il1rn—Il1r2,* and *Il1a—Il1r2* signaling converged on the mesenchymal compartment, indicating a coordinated influence from both epithelial and immune sources on mesenchymal behavior (**Fig. 6f**). These IL-1 family interactions stood out for their frequency and specificity, suggesting that regulation of IL-1 signaling represents a core organizing principle within the broader circuit. The juxtaposition of Il1a, a pro-inflammatory cytokine, with *Il1rn*, a natural antagonist that dampens IL-1 signaling, implies not just signal delivery, but a built-in regulatory logic gate—a mechanism to balance activation and resolution (Willart et al., 2012; Eislymayr et al., 2022). Rather than triggering a unidirectional fibroinflammatory response, epithelial and myeloid cells appear to activate and modulate mesenchymal engagement—adjusting the amplitude and duration of signaling to preserve tissue structure and prevent excessive remodeling.

We also identified reverse signaling from mesenchymal populations to hillock cells, including *Mdk—Tspan1, Efnb2—Ephb3*, and *Ereg—Erbb3* (**Fig. 6g**) These axes may imply that mesenchyme contributes actively to epithelial regulation, delivering cues that may support survival, polarity, and lineage plasticity. Midkine (*Mdk*) signaling through *Tspan1* could promote regenerative readiness, *Efnb2–Ephb3* interactions may help structure niche organization, and *Ereg–Erbb3* signaling likely supports proliferative or differentiative programs (Deguchi et al., 2024; Zhang et al., 2023; Lewis et al., 2022; Stahl et al., 2013). Together, these interactions frame hillock cells not as passive endpoints, but as highly receptive participants in a dynamic signaling circuit.

Beyond directionally polarized signaling, we also identified multi-nodal, reciprocal interactions engaging all three compartments. Several of these were dependent on the presence of immune cells and revealed critical immune–mesenchymal crosstalk. Macrophage-derived ligands such as *Il1a*, *Il1rn*, and *Tnf* targeted receptors *Il1r1*, *Il1r2*, and *Tnfrsf1a* on mesenchymal populations (**Fig. 6f**), establishing signaling pathways that were absent or greatly diminished in immune-depleted conditions like PD_3D. Conversely, mesenchymal subsets—including *Rspo3*$^{+}$ fibroblasts and *Pdgfrb*$^{+}$ pericytes—signaled back to immune cells via axes such as *Efnb2–Ephb3* and *Mdk–Tspan1* **(Fig. 6g),** suggesting that fibroblasts may influence macrophage adhesion, positioning, or state. These reciprocal interactions underscore that immune and mesenchymal compartments form a bidirectional signaling circuit essential to the broader regenerative niche.

Simultaneously, we observed broader multi-nodal pathways such as the *Tgfa–Egfr* axis, which exhibited robust signaling from hillock cells to all compartments—including immune cells, mesenchyme, pericytes, and back to epithelium itself (**Fig. 6h**). *Tgfa*, a potent EGFR ligand involved in epithelial proliferation and morphogenesis under stress (Korfhagen et al., 1994; Hardie et al., 2004; Buckley et al., 2008), was broadly expressed in hillock cells, while *Egfr* was distributed across hillock-like and mesenchymal populations. This pattern suggests that *Tgfa*-producing epithelial cells

may function as central broadcasting nodes, orchestrating multicellular responses through autocrine and paracrine loops. While *Tgfa–Egfr* signaling reinforces epithelial identity, it may also modulate mesenchymal responsiveness or act as a feedback hub. Other cross-compartmental axes, such as *Fn1–Itgav*, flowed predominantly from mesenchyme to epithelium and likely support matrix remodeling and epithelial repair (**Fig. 6h**)(Wang et al., 2022).

Taken together, these patterns reveal a cohesive, multi-lineage signaling circuit in which epithelial, immune, and mesenchymal populations operate in tightly integrated roles. Hillock cells emerge as central nodes—broadcasting immune- and mesenchymal-modulating signals while simultaneously responding to instructive inputs from their neighbors. The presence of shared ligands such as *Il1rn, Il1a,* and *Serpina1*, along with reciprocal mesenchymal cues via *Mdk, Efnb2,* and *Ereg*, points to a signaling architecture that is not strictly regenerative or inflammatory, but adaptive—flexibly responding to tissue context.

Ultimately, this network of interactions suggests a model in which transitional epithelial states are governed by an emergent, cross-compartmental logic—one that integrates pro-repair, pro-inflammatory, and regulatory signals across epithelial, immune, and mesenchymal compartments. Rather than operating through a top-down hierarchy, the system appears to rely on distributed signaling feedback, wherein epithelial identity, immune tone, and mesenchymal responsiveness are co-regulated in response to local context. This architecture may not ensure a return to homeostasis, but it enables tissues to adaptively recalibrate their composition and signaling dynamics in the face of perturbation. In this framework, mesenchyme is not simply permissive but actively interprets and integrates immune and epithelial inputs, shaping the structural and signaling environment in which repair unfolds.

Discussion

This study presents a compositionally defined lung organoid model capable of supporting multicellular self-organization, lineage-specific fate emergence, and microenvironmental signaling analysis. By varying the relative contribution of immune- and mesenchyme-containing inputs under uniform matrix, media, and environmental conditions, we established a platform to investigate how initial cellular composition shapes epithelial and immune dynamics. The ability to maintain cell-type diversity and track context-dependent behavior under standardized conditions enables a degree of experimental control rarely achievable in vivo and allows for interrogation of regenerative signaling at both cellular and network levels.

Notably, we observed robust epithelial expansion from bronchoalveolar lavage (BAL)–derived samples that contained only a minor fraction of epithelial cells and lacked mesenchymal populations entirely. Despite being predominantly immune in composition, these samples reproducibly gave rise to diverse epithelial lineages, including transitional and secretory subtypes, without deliberate injury cues or

progenitor enrichment. This contrasts with recent work requiring fluorescence-activated cell sorting to expand BAL-derived progenitors, highlighting the utility of unsorted lavage as a tractable source for modeling epithelial plasticity (Liu et al., 2024). Moreover, we successfully expanded both proximal and distal epithelial populations without necessitating strictly “proximal” or “distal” growth media. The generation of complex epithelial structures from trace epithelial input under defined culture conditions underscores the model’s translational potential in regenerative medicine and cell therapy development.

Across conditions, transitional epithelial states—including Sox9^{+} stressed progenitors, hillock cells, and secretory-alveolar intermediates—emerged without directed differentiation. Their appearance suggests that matrix and media alone can promote epithelial plasticity; notably, the medium used was originally designed to expand embryonic lung progenitors. However, the relative abundance and character of transitional populations varied between conditions, indicating that local niche composition—particularly the presence of immune and mesenchymal cells—also influenced epithelial remodeling. Among these states, hillock-like cells expanded with striking consistency. Their expansion here offers a unique opportunity to probe their molecular identity, functional role, and potential contributions to tissue homeostasis.

Hillock-like cells were most prominent in conditions retaining mesenchymal populations, particularly Mixed_3D and PD_3D. Their consistent emergence under defined conditions provides a model to study their role in epithelial repair, immune coordination, and pathologic remodeling. These *Krt13*$^{+}$/*Sprr1a*$^{+}$ cells exhibited stratified organization, context-specific polarization, and expression of immune-modulatory genes—features consistent with barrier-associated remodeling (Holztmann et al., 2002; Stouch et al., 2016; Zhang et al., 2023). Luminal hillock cells expressed cytokines, alarmins, and antimicrobial genes, suggesting a regulatory role at the interface of epithelial and immune compartments. To our knowledge, this is the first study to begin delineating the cell–cell signaling architecture associated with hillock cells. We identified signaling axes linking hillock cells to mesenchymal and immune partners—including *Il1a–Il1r2 and Serpina1–Lrp1*—that position these cells as both sensors and broadcasters of inflammatory and regenerative cues. Rather than passive responders or indicators of dysfunction, hillock cells may serve as active modulators of tissue recovery, helping to calibrate local inflammation and stabilize epithelial integrity (Lim et al., 2024).

RAS/AT0-like intermediates emerged most robustly in the mesenchyme-rich conditions, Mixed_3D and PD_3D. In the presence of mesenchymal-derived WNT and BMP ligands—critical signals for epithelial patterning and resolution (Frum et al., 2023; Konigshoff & Eickelberg, 2009; Ostrin et al., 2018)—may support or stabilize these transitional states. This finding aligns with emerging evidence that epithelial fate is not strictly lineage-encoded but instead fine-tuned by environmental inputs. Moreover, it supports the hypothesis that transitional states can become maladaptively stabilized under pathological conditions (Jones et al., 2024; Strunz et al., 2020). Our model

provides a tractable system to study the regulation and persistence of these intermediates.

Our findings underscore the context-responsive plasticity of macrophages and their capacity to recalibrate based on surrounding niche cues. In PD_3D and Mixed_3D, where mesenchymal components were retained, macrophages upregulated inflammatory mediators absent from starting populations, including *Il1a, Il1b, Cxcl1–3,* and *Nos2*, consistent with mesenchymal-driven inflammatory polarization (Eislmayr et al., 2022; Wang et al., 2022; Giri et al., 2020). In contrast, BAL_3D macrophages sustained or amplified programs associated with immune resolution and epithelial support, such as *Pparg, Cela1*, and *Lpl* (Lee et al., 2024; Babaev et al., 1999; Joshi et al., 2017). These results support a model in which macrophages, like hillock cells in our system, function as adaptable regulators, dynamically shaping inflammatory tone and epithelial fate through context-dependent interactions. Future studies will be needed to define the molecular mechanisms driving these shifts and their contributions to regenerative versus maladaptive trajectories.

This interpretation aligns with frameworks that conceptualize inflammation not as a mere consequence of damage, but as a regulatory mechanism that preserves tissue function through adaptive coordination (Medzhitov, 2021). From this perspective, the emergence of *Sox9*$^{+}$ progenitors, hillock-like cells, and RAS/AT0-like intermediates may represent a proactive epithelial strategy to integrate environmental signals and maintain regenerative readiness. The co-expression of stress markers such as *Cox4i2* and *Ptges* in the *Sox9*$^{+}$ population underscores their dual role in metabolic adaptation and immune modulation. Far from being artifacts of culture, these transitional states may function as context-sensitive intermediates that balance proliferation, stress response, and signaling plasticity (Warren et al., 2024). Their reproducible emergence highlights this system's potential to dissect both successful regeneration and its derailment in chronic disease.

Limitations

While our organoid model offers a powerful system to explore epithelial plasticity and intercellular signaling under defined conditions, several limitations warrant consideration.

First, while we performed single-cell RNA sequencing on our starting PD and BAL populations to define initial cell type composition, we did not prospectively enrich, deplete, or barcode individual lineages prior to culture. As such, although we can infer the presence of epithelial, immune, and mesenchymal populations at the outset, we cannot precisely determine which subsets of our starting population persisted, expanded, or underwent state transitions during organoid growth. While we did not track individual lineages prospectively, our approach allowed us to identify which cell states persisted and, more notably, to capture the emergence of transitional populations that were absent from the starting scRNA-seq profiles, highlighting the plasticity and context-dependent induction of these intermediates. Future experiments incorporating

prospective lineage tracking, genetic barcoding, or FACS-based enrichment strategies will be essential to resolve the origin and fate of constituent cell types within the regenerative circuit.

Second, our analysis was conducted at a single terminal time point (day 10). Without intermediate sampling, it remains unclear whether the transitional epithelial populations we observe—such as stressed *Sox9*$^{+}$ progenitors, hillock cells, and secretory-alveolar intermediates—represent stable endpoints or transient intermediates en route to terminal differentiation. Time-course transcriptomic profiling, in combination with trajectory inference and fate-mapping tools, will be critical to define the emergence, persistence, and resolution of these states.

Third, while we employed immunohistochemistry to confirm the presence and localization of key epithelial populations, we were unable to comprehensively validate the spatial relationships of all cell types or signaling partners—particularly among macrophage, mesenchymal, and hillock cells. This limitation stems in part from the challenges of whole-mount staining and imaging in organoids, which rapidly lose structural integrity—especially in the BAL_3D condition—and from the limited availability of high-quality rat-reactive antibodies for detection. Future application of spatial transcriptomics or high-resolution in situ hybridization approaches will be crucial to determine whether observed ligand-receptor circuits correspond to physically adjacent cell types and to define how niche topology may constrain or facilitate regenerative signaling.

Fourth, although media conditions were standardized across cultures, the inclusion of small molecule inhibitors and growth factors inherently selects for progenitor maintenance. While this design enabled controlled comparisons across compositions, it may have artificially sustained transitional states that would otherwise resolve under more restrictive conditions. Future iterative perturbation of individual signaling components will be important to define the context-dependence of observed plasticity.

Finally, while the model captures key aspects of regenerative signaling and tissue self-organization, it does not incorporate biomechanical inputs such as stretch, airflow, or perfusion—factors known to influence epithelial differentiation, cytoskeletal dynamics, and extracellular matrix remodeling. In the native lung, cyclic stretch and airflow regulate alveolar type I/II fate balance, modulate surfactant production, and contribute to progenitor cell activation (Sanchez-Esteban, 2001; Goodwin et al., 2023). Mechanical strain has also been shown to shape mesenchymal–epithelial interactions during branching morphogenesis and to condition immune behavior via mechanotransduction pathways (Ahmed et al., 2023; Shiraishi et al., 2023; Vining & Mooney, 2017). Incorporating biomechanical forces into future versions of this model—whether via microfluidic perfusion, cyclic stretch chambers, or bioreactors—may enhance physiological fidelity and yield new insight into how physical stimuli intersect with lineage composition and intercellular communication.

Future Directions

Our findings suggest that transitional cells are part of a larger regenerative logic: plastic intermediates that integrate local cues to orchestrate repair, calibrate inflammation, and potentially resist progression to disease.

These insights motivate several future questions:

- What governs the resolution or persistence of transitional states? Can *Sox9*$^{+}$ or hillock-like cells revert, differentiate, or become pathologically stabilized depending on microenvironmental context?
- Is the hillock niche an inducible, facultative module for immune–epithelial coordination in the proximal lung—or a universal regenerative structure across airway compartments? How does its formation relate to chronic remodeling in disease?
- How tightly coupled are macrophage polarization and epithelial transitions? What additional signaling circuits—beyond IL-1 family and *Serpina1* axes—mediate their coordination or decoupling?
- Can early manipulation of lineage balance redirect regenerative trajectories? How do immune or mesenchymal biases, imposed at seeding, shape the fate spectrum or likelihood of repair versus maladaptive remodeling?
- What role do biomechanical signals play in resolving or reinforcing these states? In vivo, physical inputs such as cyclic strain or shear stress may help finalize epithelial fate decisions that remain plastic in static culture. Integrating such forces into future models could offer insight into how tissue mechanics intersect with regenerative patterning.

We present these experiments and findings to the community to advance understanding of how compositional and signaling cues guide epithelial state transitions. This knowledge may open new therapeutic avenues for restoring tissue integrity in chronic lung disease.

Materials & Methods

Animal Handling and Lung Dissociation

Eight- to ten-week-old male Sprague Dawley rats (n = 6; 250 g ± 25) were sacrificed for cell collection. Rats were sedated in a chamber containing Isoflurane-soaked (20% w/v) gauze, followed by intraperitoneal administration of 0.25 mL Ketamine-Xylazine solution (K: 75 mg/mL; X: 5 mg/mL) and 0.15 mL heparin (1,000 U/mL). Once fully sedated, animals were sterilized with 70% ethanol and iodine wipes. Through the thoracic cavity, the lungs were allowed to deflate, and the thymus was removed. The clavicle was dissected to expose the trachea, which was cannulated using a barbed Y 1/16" connector. A second barbed Y 1/16" connector was used to cannulate the pulmonary artery. The cardiac apex was excised to allow fluid flow, and the lung tissue was perfused at 50 mL/min with heparin (100 U/mL) and sodium nitroprusside (SNP; 0.1 mg/mL). The lungs were then excised and placed in a petri dish for perfusion with dissociation buffer (DMEM HG [Gibco], 1 mg/mL Collagenase/Dispase [Roche], 3 U/mL Elastase [Worthington], 20 U/mL DNase) through both the airway and vasculature via gravity. A total of 10 mL of dissociation buffer was used to inflate the lungs three times. The lungs were transferred to conical tubes containing dissociation buffer and incubated on a rocker at 37°C for 25 minutes. All animal procedures were conducted in accordance with Yale Institutional Animal Care and Use Committee (IACUC).

Pulmonary Dissociation Cell Isolation and Processing

Following enzymatic digestion, cells were dissociated from the lung tissue using a spatula and passed through a strainer, leaving behind larger collagenous structures. The strainer was rinsed with 20 mL of quenching medium (DMEM HG (Gibco, 11965092), 10% FBS, 1% P/S (Worthington), 0.1% gentamycin (Worthington), 1% ampicillin (Worthington,)), and the resulting cell suspension was collected. The suspension was centrifuged at 300 g for 5 minutes at 4°C, and the supernatant was discarded. The cell pellet was resuspended in an equal volume of ACK Lysing Buffer (Gibco, A1049201) and agitated manually at room temperature for 2 minutes. The suspension was diluted with 10 mL of MACS buffer (0.1% BSA [Gemini] in PBS [Gibco], filtered), followed by centrifugation at 300 g for 5 minutes at 4°C. The supernatant was aspirated, and the pellet was resuspended in 5 mL of MACS buffer. The suspension was sequentially filtered through 70 µm and 40 µm strainers (Falcon, 352350, 352340) to remove debris. Cells were pelleted by centrifugation at 300 g for 5 minutes at 4°C, and the supernatant was removed. The pellet was resuspended in 5 mL of MACS buffer, filtered twice through a 40 µm strainer, and counted. Finally, the cells were resuspended in the 1 mL of MACS buffer per 10^7 total cells before proceeding to cell selection with Dclk1$^+$ tagged beads.

Preparation of Anti-Dclk1–Tagged Magnetic Beads

Magnetic beads were prepared using 1 mg (100 µL) of M-280 Sheep anti-Rabbit IgG Dynabeads (ThermoFisher, 11203D) suspended in 500 µL of MACS buffer (0.1% BSA [GEMINI, 700-100P] in PBS [Gibco, 14190144]). The suspension was placed in a DynaMag™-5 Magnet (ThermoFisher, 12303D) for 1 minute to separate the beads, and the supernatant was aspirated. This washing step was repeated three times, with resuspension in 500 µL of MACS buffer each time. After the final wash, Dynabeads were resuspended in MACS buffer, and 10 µg of anti-Dclk1 antibody (Abcam, ab31704) was added to achieve a final volume of 100 µL. The volume of the antibody solution was adjusted based on the supplied concentration. The bead-antibody mixture was incubated at room temperature for 30 minutes with gentle tilting and rotation. Following incubation, 500 µL of MACS buffer was added, and the suspension was pipetted up and down several times. The beads were washed three additional times with MACS buffer using the DynaMag™-5 Magnet. The final bead suspension was resuspended in 100 µL of MACS buffer and stored at 4°C for no more than 24 hours before use.

Cell Type Enrichment with Dclk1+ Tagged Beads

Pulmonary dissociation cells in 1 mL of MACS buffer per 10^7 total cells were strained through a 40 µm cell strainer (Falcon, 352340) to remove cell aggregates. Dynabeads prepared with anti-Dclk1 antibody were added at a concentration of 25 µL per 10^7 total cells. The cell-bead mixture was incubated at 4°C for 30 minutes with gentle tilting and rotation using a tube mixer to prevent bead settling. Following incubation, the suspension volume was doubled with MACS buffer to minimize trapping of unbound cells. Tubes were placed in the DynaMag™-5 Magnet under aseptic conditions for 2 minutes, and the supernatant was carefully aspirated. The bead-bound cells were washed with 1 mL of MACS buffer, followed by an additional magnetic separation for 1 minute. This washing step was repeated four times to maximize enrichment. The final cell pellet was resuspended in MACS buffer to detach any adhered cells from the tube walls and centrifuged at 300 g for 5 minutes at 4°C. After aspirating the supernatant, the cells were resuspended in LPM-3D medium to achieve the desired concentration for organoid plating.

Bronchoalveolar Lavage (BAL) Cell Collection

Bronchoalveolar lavage (BAL) cells were collected from 8–10-week-old male Sprague Dawley rats (n = 3; 250 g ± 25), following the same sacrifice protocol outlined in the methods section *Animal Handling and Lung Dissociation***.** After tissue extraction, the lungs were placed in a conical tube containing 40 mL of ice-cold saline solution (PBS, 1% P/S) and kept on ice for 60 minutes. Following incubation, the lungs were perfused through the trachea with saline solution to achieve maximal inflation, followed by gentle tissue massage. Negative pressure was created by covering the open end of the tracheal cannula, and the saline solution was aspirated using a syringe. This lavage

process was repeated 5–7 times, with all aspirated fluid collected into a sterile 50 mL conical tube.

The collected lavage suspension was centrifuged at 500 g for 10 minutes at 4°C. After centrifugation, the supernatant was aspirated, and the pellet was resuspended in an equal volume of ACK lysing buffer (Gibco, A1049201)(1:1 ratio). The pellet was manually agitated for 2 minutes at room temperature before dilution with 2 mL of DMEM supplemented with 10% FBS. The final cell suspension was counted and resuspended to the desired concentration for organoid seeding.

Organoid Culture

Organoid cultures were established in 0.4 µm, 24-well cell culture inserts (Falcon) using a 1:1 (v/v) ratio of growth factor-reduced Matrigel (Corning, Matrigel GFR, Phenol Red-Free, #356231) to cell suspension. Each transwell insert contained a total volume of 150 µL, consisting of 45 µL Matrigel and 45 µL cell suspension. All organoid suspensions were prepared using LPM-3D medium and maintained at 37°C. The following cell seeding densities were used: PD_3D (0.1×10^6 cells from PD), Mixed_3D (5×10^4 PD cells and 5×10^4 BAL cells), and BAL_3D (0.1×10^6 cells from BAL). Organoid suspensions were prepared on dry ice, and chilled, wide-bore pipette tips were used for sample distribution to ensure consistent handling. Large bubbles in the Matrigel were removed using sterile needles prior to solidification. Following a 30-minute incubation at 37°C, 500 µL of culture medium was added to the basolateral compartment of the Transwell system. Media changes were performed every 48 hours across all conditions. Biological replicates were prepared for each condition (n=18, with n=6 per experiment). Organoids were maintained in culture for 10 days at 5% CO_2 at 37°C. Organoids used for scRNAseq were dissociated on day 10 following the methods outlined in methods section *Organoid Dissociation.*

Organoid Dissociation

Organoids were dissociated using a customized enzymatic digestion protocol. The culture medium was removed, and 1 mL of ice-cold DPBS (Gibco, 14190144) was added to each well. The growth factor-reduced Matrigel (Corning, Matrigel GFR, Phenol Red-Free, #356231) matrix was disrupted by gently pipetting the suspension up and down approximately 20 times using a P1000 wide-bore pipette coated with BSA. The organoid suspension was transferred to a 15 mL conical tube coated with anti-adherence solution and centrifuged at 300g for 5 minutes at 4°C to pellet the organoid-cell suspension. The supernatant was aspirated, and the pellet was washed with 0.5 mL of ice-cold DPBS to remove residual Matrigel before enzymatic dissociation.

The pelleted organoids were resuspended in 1 mL of dissociation enzyme solution, consisting of DMEM HG (Gibco, 11965092), 1 mg/mL Collagenase/Dispase (Roche, 11097113001), 3 U/mL Elastase (Worthington, LS002292), and 20 U/mL DNase. The suspension was incubated at 37°C on an orbital shaker to provide gentle agitation and facilitate dissociation while minimizing mechanical stress. After 20-25 minutes of

incubation, the suspension was gently pipetted up and down 5–10 times using a wide-bore pipette to achieve a single-cell suspension.

To terminate enzymatic activity, 10 mL of Advanced DMEM/F12 medium (ThermoFisher, 12634010) was added to the cell suspension. The cells were then filtered through a 100 µm cell strainer (Corning, 431752), using the rubber head of a 5 mL syringe plunger to gently push any remaining cell aggregates through the strainer. The suspension was again centrifuged at 300g for 5 minutes at 4°C, and the supernatant was discarded. The pellet was again resuspended in 5 mL of LPM-3D medium and filtered through a 70 µm cell strainer (Corning, 431751), using a clean syringe plunger to push remaining aggregates through. The filtered suspension was centrifuged at 300g for 5 minutes at 4°C one final time before being filtered through a 40 µm cell strainer (Corning, 431750) to ensure a single-cell suspension. Cells were then counted to determine concentration and ensure viability before being processed for downstream applications. Samples dissociated for single-cell RNA sequencing were resuspended at 1 million cells/mL in 0.1% BSA in PBS. Cells to be cryopreserved were resuspended in the desired volume of freezing medium (90% FBS (Hyclone, SH30071), 10% DMSO (Sigma, C6295)) before being transferred to -80 °C for no more than 24 hours and then the cryogenic dewar for longer-term storage.

Organoid and Tissue Fixation

Native Rat Lung

Native rat lungs were perfused with 4% paraformaldehyde (PFA) at a flow rate of 60 mL/min for a minimum of 12 hours. After fixation, the lungs were transferred to a sterile petri dish for dissection. Anatomical dissection was performed to ensure that each lobe and the trachea were embedded individually. Tissue embedding and sectioning were performed by Yale Pathology Tissue Services (YPTS).

Organoids

Organoids were fixed using one of three methods, depending on the intended downstream application.

For organoids embedded and sectioned with the Transwell membrane, cell culture media was removed, and 0.5 mL of 4% PFA was added to the basolateral compartment of the Transwell insert. The plate was placed on a rocker for 16 hours without prior Matrigel digestion. After 12 hours of incubation, the Transwell membrane containing the Matrigel-embedded organoids was excised using a scalpel. The excised membrane was embedded in HistoGel before paraffin embedding and sectioning by Yale Pathology Tissue Services (YPTS).

For organoids embedded without Matrigel, the organoids were first washed with ice-cold PBS and placed on an orbital shaker at 4°C for 60 minutes. Organoids were then collected in PBS using a P1000 wide-bore pipette coated with BSA to prevent adherence to the pipette tip. The collected organoids were centrifuged in a 15 mL conical tube coated with BSA at 200g for 3 minutes at 4°C. The supernatant was carefully aspirated to avoid loss of organoids, and the pellet was resuspended in 2 mL of 4% PFA. Fixation was carried out on a rocker for 4 hours at room temperature. Following fixation, PFA was aspirated, and the organoids were embedded in a droplet of HistoGel prior to paraffin embedding and sectioning by Yale Pathology Tissue Services (YPTS).

For organoids undergoing whole-mount staining, the same preparation steps as those used for organoids embedded without Matrigel were followed. However, instead of HistoGel embedding, the organoids were resuspended in PBS after fixation and transferred to 4-well chamber slides (ThermoFisher, Nunc Lab-Tek II) for subsequent staining and imaging.

LPM-3D Media Preparation

Epithelial expansion medium was prepared as previously described, with minor modifications (Nichane et al., 2017). Briefly, Advanced DMEM/F12 basal medium (ThermoFisher, 11320033) was filtered and supplemented with the following rat growth factors: FGF10 (50 ng/mL; R&D Systems, 7804-FG), FGF9 (50 ng/mL; R&D Systems, 273-F9), and EGF (50 ng/mL; R&D Systems, 3214-EG) (**Supplementary Table 1 (S1)**). Additionally, the medium was supplemented with small molecule inhibitors, including CHIR99021 (3 μM; GSK-3 inhibitor/Wnt activator; Cayman Chemical, 13122), BIRB796 (1 μM; p38-MAPK inhibitor; Cayman Chemical), Y27632 (10 μM; ROCK inhibitor; Cayman Chemical, 10460), and A8301 (1 μM; Activin/NODAL/TGF-β pathway inhibitor; Cayman Chemical, 9001799). Further supplements included heparin (5 μg/mL; Sigma Aldrich, 9041-08-1), insulin (10 μg/mL; Roche), and transferrin (15 μg/mL; Roche). The prepared medium was pre-warmed to 37°C before application to cell cultures. Antibiotics were added at final concentrations of 1% penicillin-streptomycin (P/S) and 0.1% gentamicin to prevent contamination.

Immunohistochemistry of Paraffin Embedded Sections

Paraffin embedded sections of perfused native rat lung, trachea, and pulmonary organoid systems blocked and sectioned by YPTS were processed for immunostaining to localize protein expression. Samples were first deparaffinized by heating at 65°C for 30 minutes, followed by sequential rinsing in a xylene and ethanol gradient (100%, 95%, and 70% ethanol). Antigen retrieval was performed by immersing the slides in antigen retrieval buffer (0.1 M citric acid, 0.05% Tween 20, pH 6) at 75°C for 20 minutes, followed by gradual cooling to room temperature. Two different permeabilization buffers were utilized depending on the target stains. For nuclear stains (e.g. transcription factors such as Sox9), tissue sections were permeabilized using PBS supplemented

with 0.2% Triton-X (Invitrogen, HFH10) for 15 minutes. After permeabilization, samples were blocked with blocking buffer (0.75% glycine, 5% BSA in PBS) for 1 hour to minimize nonspecific binding. For cell surface and cytoplasmic markers, tissue sections were permeabilized with 0.5% Tween-20 (Millipore, P1379) in PBS for 15 minutes, followed by the same blocking buffer step described previously. Primary antibodies, prepared in the same blocking buffer, were applied to the samples at their respective concentrations and incubated overnight at 4°C. Following incubation, slides were washed 3–5 times with PBS before the application of secondary antibodies for 1 hour at room temperature. Slides were washed again with PBS and counterstained with DAPI (Invitrogen, D1306) (1:1000 in PBS) for 1 minute to visualize nuclei. Finally, sections were mounted using PVA-DABCO (Sigma Aldrich,10981). Details of all primary and secondary antibodies used are provided in **Supplementary Tables 2 (S2) and 3 (S3),** respectively.

Immunofluorescence of Starting Population Cytospins

Cytospins were generated for all three starting populations (BAL, PD, and a 1:1 mix of the two that subsequently became Mixed_3D). Slides were securely placed in the slide holder, ensuring proper orientation with the frosted side of the slide facing upwards. A filter card, with its absorbent side against the slide, was positioned alongside the cytofunnel, ensuring proper alignment of all components before securing the holder. Each assembled holder was then placed in the Cytospin centrifuge (Cytospin 4 Centrifuge, ThermoScientific). Each cell suspension, prepared at a concentration of 0.5 × 10^6 cells/mL in DMEM + 10% FBS, was pipetted into each cytofunnel as a 200 µL volume. The slides were centrifuged at 1000 × g for 5 minutes. Following centrifugation, slides were removed from the centrifuge and taken out of the holders. Slides were placed cell-side up and left to air-dry for 1 hour. Spots containing cell suspensions were outlined with a hydrophobic marker (ReadyProbes™ Hydrophobic Barrier Pap Pen; ThermoFisher) before being fixed with 4% paraformaldehyde in PBS for 10 minutes at room temperature. After fixation, slides were rinsed 3 times with PBS and stored in PBS at 4°C until needed for staining (up to one week). Slides were processed as described in the previous section from the antigen retrieval step onward.

Organoid Image Analysis & Quantification

Time course brightfield images of each condition (n=3) were taken at days 0, 3, 5, 7, and 9 using the EVOS FL Auto 2 microscope. Stitched images of each well were generated. Following image acquisition, images were analyzed using QUPath (v.0.5.1). Organoid areas in stitched images at each time point were recorded using both the ellipse and brush tools in QUPath. To enable real-world area quantification (µm²), image scale was calibrated in QuPath using the embedded 1 mm scale bar present in each stitched image. The number of pixels spanning the scale bar was measured using Fiji (ImageJ), and this value was used to calculate the corresponding microns-per-pixel ratio. This scale was then manually entered into QuPath's image properties to ensure that all organoid area measurements reflected true physical dimensions. Organoid

count and area values were averaged across replicates per condition and timepoint. Time was converted to hours, and line plots were generated showing mean values ± standard deviation. Welch's t-tests were used to compare conditions at each timepoint for both organoid count and area, without assuming equal variance. Resulting *p*-values were adjusted using the Benjamini–Hochberg (BH) method to control the false discovery rate. Statistical significance was denoted as follows: $p \leq 0.05$ (*), ≤ 0.01 (**), ≤ 0.001(***).

Single-Cell RNA Sequencing Library Preparation and Quality Control

Library Prep

Dissociated organoid and cell suspensions were prepared for single-cell RNA sequencing using the Chromium Next GEM Single Cell 3' Reagent Kits v3.1 (10x Genomics, Pleasanton, CA). Following dissociation, cells were counted, assessed for viability, and resuspended at a concentration of 1 million cells/mL in 0.1% BSA in PBS before proceeding to library preparation.

For library preparation, cell suspensions were combined with the Master Mix containing reverse transcription (RT) reagents and loaded into a Chromium Next GEM Chip G, along with Partitioning Oil and barcoded Gel Beads. The Chromium Controller was used to generate Gel Beads-in-emulsion (GEMs), with each GEM encapsulating a single cell and a barcoded Gel Bead. Gel Beads contained primers with a unique 16-nucleotide 10x Barcode, a 12-nucleotide unique molecular identifier (UMI), and a poly(dT) sequence for mRNA capture.

Following GEM formation and barcoding, GEMs were incubated at 53°C for 45 minutes to allow reverse transcription of poly-adenylated mRNA into cDNA. After incubation, GEMs were broken, and barcoded full-length cDNA was recovered. Purification was performed using Dynabeads MyOne SILANE magnetic beads (Invitrogen, 37002D) to remove unused primers, enzymes, and partitioning oil.

Purified cDNA was then amplified via PCR to generate sufficient yield for downstream processing. Amplified cDNA was purified using SPRIselect beads (Beckman Coulter, NC0406406) to remove unwanted shorter fragments and contaminants.

After cDNA purification, sequential enzymatic reactions were performed to prepare the cDNA for sequencing. First, the amplified cDNA was enzymatically fragmented to generate appropriately sized fragments, followed by end repair and A-tailing to prepare for adaptor ligation. Next, adaptors were ligated to the cDNA fragments, enabling efficient amplification in subsequent steps. Then, PCR amplification of the final libraries was performed to obtain sufficient material for sequencing. Finally, a double-sided SPRIselect bead-based size selection was conducted to enrich fragments in the 200–9000 bp range, ensuring optimal performance in downstream sequencing.

Quality Control

The quality and concentration of amplified cDNA were assessed using an Agilent 2100 Bioanalyzer High Sensitivity DNA Kit, while quantification was performed with a Qubit 4.0 Fluorometer using the Qubit dsDNA HS Assay Kit.

Post-library construction, libraries underwent additional quality control using the Agilent 4200 TapeStation, where the fragment size distribution was assessed. The final library concentrations were measured using the KAPA Library Quantification Kit to ensure accurate input amounts for Illumina sequencing platforms.

Libraries were sequenced by the Yale Center for Genomic Analysis (YCGA) at a target recovery of 2,000-10,000 cells per sample, and a target depth of 50,000 reads/cell on an Illumina NovaSeq 6000. Sequencing data was processed using Cell Ranger (v8.0.1). The reference transcriptome used for alignment was Rattus norvegicus.Rnor_6.0-95. Alignment was performed with the "-include – introns" option enabled, allowing both exonic and intronic reads to be considered for gene expression quantification.

Single-Cell Data Processing and Analysis

Single-cell RNA sequencing (scRNA-seq) data were processed individually for each sample using the Seurat package (version 5.2.0), following best practices (Luecken & Theis, 2019). Raw sequencing data were read into R using the Read10X function, and Seurat objects were created for each sample with a minimum of 3 cells and 50 features. Quality control metrics were calculated, including the percentage of mitochondrial gene content (percent.mt), total unique molecular identifier (UMI) counts (nCount_RNA), and detected features (nFeature_RNA). Sample-specific filtering thresholds for nCount_RNA and nFeature_RNA were applied as detailed in **Supplemental Table 4 (S4).**

Initial quality control (QC) was performed to remove low-quality cells based on mitochondrial gene expression and unique feature counts. Cells with high mitochondrial percentages or low feature counts were excluded from further analysis. To ensure accurate identification and removal of low-information cells, an initial clustering step was performed at a high resolution (e.g., res = 5.0) to finely delineate clusters. This allowed us to identify and remove clusters with low gene expression variability or high proportions of ambient RNA contamination. Once low-information cells were filtered out, we re-clustered the remaining cells at an optimized resolution to obtain biologically meaningful clusters. QC plots for the starting BAL population can be found in **Supplemental Fig. 5**. QC plots for the starting PD population can be found in **Supplemental Fig. 6**. QC plots for the organoid sequencing data (merged) can be found in **Supplemental Fig. 4**.

Dimensionality reduction was conducted using principal component analysis (PCA), followed by Uniform Manifold Approximation and Projection (UMAP) for visualization. Clustering was performed using the Louvain algorithm implemented in Seurat. UMAP dimensionality reduction was performed using RunUMAP with the selected principal components, followed by construction of a shared nearest neighbor (SNN) graph using FindNeighbors. Clustering was conducted using the FindClusters function—a Louvain

algorithm implemented in Seurat—with a range of resolution values to achieve optimal clustering granularity.

Differential Expression Analysis

To identify marker genes for each cluster, differential expression analysis was performed using FindAllMarkers with a minimum percentage threshold of 0.1 and log-fold change threshold of 0.1. Top markers were selected based on power metrics (ratio × log-fold change), and heatmaps were generated to visualize cluster-specific expression patterns.

Cell Type Annotation

Cell type annotation was conducted using multiple reference datasets and marker-based approaches. Prior to cell type annotations, clusters were grouped by cell class, using the following canonical markers: *Epcam* (epithelium), *Col1a1* (mesenchyme), *Ptprc* (immune), and *Cdh5* (endothelium). Following this, cell type annotations were guided by an in-house adult mouse lung atlas, derived from integrating scRNAseq data from male and female mouse tissues (Obata et al., 2024). Additionally, we leveraged publicly available single-cell transcriptomic atlases, including LungMAP (Ardini-Poleske et al., 2017) and PanglaoDB (Franzén et al., 2019), which provide comprehensive reference datasets for pulmonary and general tissue-specific cell populations, respectively. LungMAP, a curated repository of developing and adult lung transcriptomes, was utilized to cross-reference canonical markers and transcriptional signatures of pulmonary cell types, ensuring consistency with established annotations of epithelial, mesenchymal, immune, and endothelial lineages. This was achieved by integrating our dataset with the LungMAP reference profiles and performing correlation-based analyses to validate our clustering assignments. Similarly, PanglaoDB, an extensive database of single-cell RNA-seq datasets across multiple tissues, was employed to confirm the broader classification of immune and stromal cell types by comparing expression patterns of conserved marker genes identified in our clusters with those reported in the database. Justifications for cell type annotations (by gene expression) for our three main single-cell objects can be found in **Supplemental Figs. 1** (BAL), **2** (PD), and **7** (Organoids: BAL_3D, Mixed_3D, PD_3D).

Canonical marker genes were used to classify cell types into broad categories such as epithelium, mesenchyme, immune, and endothelium. Specific populations, such as the 'Stressed_Progenitors', were identified by also using gene set enrichment analysis of upregulated genes in that cluster of cells. Final annotations were validated using feature plots and differential gene expression analysis using our global (merged) Seurat object of all three organoid conditions (n=3 for each condition). R markdown files walking through the cleaning, clustering, and annotation process for each sample can be found on our GitHub repository: https://github.com/RaredonLab/Edelstein2025.

Gene Set Enrichment Analysis (GSEA) with the Molecular Signatures Database (MSigDB)

To characterize transcriptional programs distinguishing basal and luminal hillock cells within the proximal epithelial subset, we performed gene set enrichment analysis (GSEA) using the Hallmark gene sets from MSigDB (v7.5.1, Broad 2022 release; Liberzon et al., 2015). Differential expression analysis was conducted on pseudobulk comparisons between BAL_3D (basal hillock-enriched) and PD_3D/Mixed_3D (luminal hillock-enriched) conditions. Genes were ranked by $\log_2$ fold-change (avg_log2FC), with gene symbols as names and missing values excluded. Rankings were supplied to the GSEA() function in the clusterProfiler package using the Hallmark gene sets obtained via msigdbr for Rattus norvegicus (Wu et al., 2021). Significantly enriched pathways were defined as those with adjusted p-values < 0.05.

To further interpret pathway content, core enriched genes for each significant term were annotated using curated ground truth gene lists. Ligands were obtained from the NICHES rat dataset (Raredon et al., 2023), matrix proteins were selected from MatrisomeDB categories "ECM Glycoproteins," "Collagens," and "Proteoglycans" (Shao et al., 2020), and transcription factors were identified from AnimalTFDB (Shen et al., 2023). Each pathway was annotated with the count and identity of ligands (excluding matrix proteins), matrix-associated genes, and transcription factors present in its leading-edge gene set. A positive normalized enrichment score (NES) indicated enrichment in basal hillock cells, whereas a negative NES indicated enrichment in luminal hillock cells.

Pseudotime Analysis

Trajectory and differential gene expression analyses were conducted using both Monocle3 and Slingshot to investigate cellular transitions within emergent populations, including hillock and pro-/anti-inflammatory macrophages. The combination of these methods provided robust validation of lineage relationships and transcriptional dynamics across multiple datasets.

Monocle3 Analysis

Monocle3 (v1.3.7) was utilized to infer cellular trajectories and identify key transcriptional changes (Cao et al., 2019). Previously processed Seurat objects for each emergent population were used as input. Raw gene expression counts, and associated cell metadata were extracted from the Seurat objects, and a Monocle3 cell data set (CDS) was constructed with gene annotations.

Dimensionality reduction embeddings, including principal component analysis (PCA) and uniform manifold approximation and projection (UMAP), were transferred from the Seurat object to the Monocle3 CDS to maintain consistency across analyses. Parameters were set based on the Seurat subset being studied.

Hillock Subset

Cells were clustered using Monocle3's clustering algorithm with a minimum branch length of 8 to minimize short, noisy branches. A Euclidean distance ratio of 2.1 and a geodesic distance ratio of 2.1 were applied to optimize trajectory learning, with the graph pruning function enabled to remove spurious connections. Cells were ordered along the inferred trajectory to model their progression through biological states, and pseudotime values were extracted and incorporated into the original Seurat metadata.

Engineered Macrophage Polarization Subset

Differential gene expression analysis was performed along the pseudotime trajectory using Moran's I test with a statistical significance threshold set at a false discovery rate (FDR) of < 0.05. Genes were ranked based on their q-values and prioritized using Moran's I statistic to identify key regulators of cellular transitions. Genes of interest were analyzed for their dynamic expression patterns across pseudotime. Trajectory plots were generated to visualize temporal expression trends. Monocle3 analysis scripts are available in our GitHub repository.

Slingshot Analysis

Slingshot (*v2.10.0*) was employed to independently verify the Monocle3 trajectory results by fitting principal curves to the UMAP-reduced space (Street et al., 2018). Subset Seurat objects of emergent populations were converted to SingleCellExperiment (SCE) format to facilitate compatibility with Slingshot. PCA and UMAP embeddings were transferred from the Seurat objects, and the cluster labeled "Cycling" was designated as the starting cluster for pseudotime ordering (Hillock analysis).

Slingshot inferred lineage relationships using cluster-based lineage tracing guided by the cell type annotations, with default smoothing splines applied to fit the trajectory curves. Pseudotime values were extracted and incorporated into the Seurat metadata for downstream comparisons with Monocle3-based pseudotime trajectories.

Differential gene expression analysis along Slingshot-derived trajectories was conducted using TradeSeq (v1.16.0). Genes expressed in at least 1% of cells with counts greater than 5 were retained for analysis (Van den Berge et al., 2020). The optimal number of knots for smoothing was determined by evaluating models across a range of 3 to 15 knots, with 15 knots selected based on the Akaike Information Criterion (AIC). An association test was performed to identify genes significantly associated with pseudotime (FDR < 0.05), and a start-vs-end test was conducted to assess gene expression changes between early and late pseudotime states. Slingshot analysis scripts are available in our GitHub repository.

Cell—Cell Connectomic Analysis with NICHES

NICHES (v0.2.3) was used to infer ligand–receptor-mediated cell–cell communication across experimental conditions. All analyses were conducted in R (v4.2.2) using Seurat (v4.3.0) and SeuratWrappers (v.0.4.0). Global NICHES analysis was performed on an integrated Seurat object of all engineered cells (PD_3D, Mixed_3D, BAL_3D, 12 samples total; n = 3 per condition). A subset analysis was conducted on a subset of object specific populations of interest to afford a finer analysis of cell-cell connectomics.

Global Analysis

Cells were first subset by condition and split by replicate (Orig_ID). For each replicate, cell–cell signaling was inferred using the RunNICHES function with the FANTOM5 ligand–receptor database and the Rnor_6.0 rat reference genome. We enabled only the CellToCell inference mode to focus on direct intercellular signaling. Outputs were merged across replicates and combined using JoinLayers. Cells with low signaling information (nFeature_CellToCell < 60) were removed. The resulting object was normalized, scaled, and run through PCA (100 components). UMAP embedding and unsupervised clustering were performed using the top 18 principal components (resolution = 0.4). To correct for batch effects, RPCA integration was performed by condition (PCs 1–16, 18–19) and by sample (PCs 1–14, 16–18). The final integrated object (eng.CTC.final) served as the basis for downstream signaling analyses. The script for this analysis can be found in our GitHub repository.

Focused Subset Analysis

To study regenerative signaling in more detail, a focused analysis was performed on a subset of six cell populations from our condition-level annotations: Hillock_Luminal, Hillock_Basal, Rspo3+_Mes, Pdgfrb+_Pericytes, Anti_Inflamm_Mac, and Pro_Inflamm_Mac. These subsets were extracted from our global, node-aligned object. Following normalization and feature selection, PCA was performed, and PCs 1:5, 7, 9–12, and 14 were used for UMAP and clustering (resolution = 0.4). NICHES was then run per replicate for each condition. Cell types with fewer than two cells per replicate were excluded. Merged CellToCell results were filtered to retain cells with ≥40 features and processed using PCA (PCs 1:10, 13–14, 17–18, 21, 23), UMAP, and clustering. The final object (regen.subset_CTC_byCondition) was used for downstream visualization and differential signaling analysis using a composite "power" metric (avg_log2FC × expression ratio). The script for this analysis can be found in our GitHub repository.

Cell Circuit-Level Visualization

To visualize prioritized signaling mechanisms as directed multicellular circuits (**Fig. 6**), we used the CircuitPlot from the NICHESMethods GitHub repository (Raredon et al., 2023; Greaney et al., 2024). This function employs a custom plotting engine (ggCircuit) that combines trigonometric positioning with ggplot2 rendering. Ligand–receptor interactions (e.g., *Il1a—Il1r2*) were visualized as directional arrows connecting cell types

defined by a metadata grouping variable (e.g., CellClass) (Wickham, 2010). Edge aesthetics reflected connection strength. Optional parameters included graph.angle, offset, and unity.normalize for layout customization. All circuits were generated from the subset connectomic object (regen.subset_CTC_bySample) using annotations from CellType.regen.spec to ensure consistency in node identity and classification.

Data Availability

Raw FASTQ files, extracted digital gene expression matrices, and all R objects, containing relevant meta-data, used in this manuscript are available at Gene Expression Omnibus GEO *******. Scripts used for the analysis and figures have been made publicly available on GitHub at https://github.com/RaredonLab/Edelstein2025.

Funding

This research was supported by laboratory startup funding to M.S.B.R. from the Yale School of Medicine and the Yale Department of Anesthesiology. The work on this study was supported in part by grant T32GM086287 from the National Institute of General Medical Sciences (NIGMS). The opinions expressed are those of the authors and do not necessarily represent the thoughts or opinions of NIGMS, NIH, or the United States government. Additional funding was provided by grant 20KK0255 from the Japan Society for the Promotion of Science.

Acknowledgments

We would like to thank Yale Center for Genome Analysis (YCGA), the Yale Pathology Tissue Services (YPTS), and Yale Center for Research Computing (YCRC) for their efforts in making this work possible. We would also like to acknowledge Dr. Allison Greaney and Dr. Themis Kyriakides for their feedback and support in story craft, single-cell analysis methodology, and overall mentorship.

Author Contributions

Conceptualization: S.E.E., M.S.B.R, S.M., M.S.; Methodology: S.E.E., M.S.B.R., S.M., H.K., N.W.; Software: S.E.E., M.S.B.R., N.W., H.K.; Validation: N.W., H.K., S.M., C.H.; Formal Analysis: S.E.E., N.W., M.S.B.R; Investigation: S.E.E., S.M., M.T.G, C.D.; Resources: M.S.B.R; Writing (Original Draft): S.E.E., M.S.B.R; Writing (Review & Editing): S.E.E., M.S.B.R., M.S., V.L., C.H., C.D.

Declaration of Interests

M.S.B.R. holds stock in and consults for Humacyte Inc., a regenerative medicine company. Humacyte did not influence the conduct, description, or interpretation of the findings in this report.

References

Abo, K. M., Sainz, J., Lindstrom-Vautrin, J., Konstantinos–Dionysios Alysandratos, Richards, A., García, C., Huang, J., Hix, O. T., Werder, R. B., Bullitt, E., Hinds, A., Falconer, I. B., Villacorta-Martin, C., Jaenisch, R., Kim, C. F., Kotton, D. N., & Wilson, A. (2022). Air-liquid interface culture promotes maturation and allows environmental exposure of pluripotent stem cell–derived alveolar epithelium. JCI Insight, 7(6). https://doi.org/10.1172/jci.insight.155589

Ahmed, D. W., Eiken, M. K., DePalma, S. J., Helms, A. S., Zemans, R. L., Spence, J. R., Baker, B. M., & Loebel, C. (2023). Integrating mechanical cues with engineered platforms to explore cardiopulmonary development and disease. *iScience*, 26(12), 108472–108472. https://doi.org/10.1016/j.isci.2023.108472

Alysandratos, K.-D., Herriges, M. J., & Kotton, D. N. (2021). Epithelial Stem and Progenitor Cells in Lung Repair and Regeneration. *Annual Review of Physiology*, 83(1), 529–550. https://doi.org/10.1146/annurev-physiol-041520-092904

Antón, O., Batista, A., Millán, J., Andrés-Delgado, L., Puertollano, R., Correas, I., & Alonso, M. A. (2008). An essential role for the MAL protein in targeting Lck to the plasma membrane of human T lymphocytes. *Journal of Experimental Medicine*, 205(13), 3201–3213. https://doi.org/10.1084/jem.200805

Ardini-Poleske, M. E., Clark, R., Ansong, C., Carson, J. A., Corley, R. A., Deutsch, G. H., Hagood, J. S., Kaminski, N., Mariani, T. J., Potter, S. R., Pryhuber, G. S., Warburton, D., Whitsett, J. A., Palmer, S. M., & Namasivayam Ambalavanan. (2017). LungMAP: The Molecular Atlas of Lung Development Program. *American Journal of Physiology-Lung Cellular and Molecular Physiology*, 313(5), L733–L740. https://doi.org/10.1152/ajplung.00139.2017

Babaev, V. R., Fazio, S., Gleaves, L. A., Carter, K. J., Semenkovich, C. F., & Linton, M. F. (1999). Macrophage lipoprotein lipase promotes foam cell formation and atherosclerosis in vivo. *Journal of Clinical Investigation*, 103(12), 1697–1705. https://doi.org/10.1172/jci6117

Barnes, J. L., Yoshida, M., He, P., Worlock, K. B., Lindeboom, R. G. H., Suo, C., Pett, J. P., Wilbrey-Clark, A., Dann, E., Mamanova, L., Richardson, L., Polanski, K., Pennycuick, A., Allen-Hyttinen, J., Herczeg, I. T., Arzili, R., Hynds, R. E., Teixeira, V. H., Haniffa, M., & Lim, K. (2023). Early human lung immune cell development and its role in epithelial cell fate. *Science Immunology*, 8(90), eadf9988. https://doi.org/10.1126/sciimmunol.adf9988

Basil, M. C., Cardenas-Diaz, F. L., Kathiriya, J. J., Morley, M. P., Carl, J., Brumwell, A. N., Katzen, J., Slovik, K. J., Babu, A., Zhou, S., Kremp, M. M., McCauley, K. B., Li, S., Planer, J. D., Hussain, S. S., Liu, X., Windmueller, R., Ying, Y., Stewart, K. M., & Oyster, M. (2022). Human distal airways contain a multipotent secretory

cell that can regenerate alveoli. *Nature*, 604(7904), 120–126. https://doi.org/10.1038/s41586-022-04552-0

Block, G. J., Ohkouchi, S., Fung, F., Frenkel, J., Gregory, C., Pochampally, R., DiMattia, G., Sullivan, D. E., & Prockop, D. J. (2009). Multipotent stromal cells are activated to reduce apoptosis in part by upregulation and secretion of stanniocalcin-1. *Stem Cells*, 27(3), 670–681. https://doi.org/10.1002/stem.20080742

Burri, P. H. (1974). The postnatal growth of the rat lung. 3. *Morphology*. The Anatomical Record, 180(1), 77–98. https://doi.org/10.1002/ar.1091800109

Cai, X. T., Jia, M., Heigl, T., Shamir, E. R., Wong, A. K., Hall, B. M., Arlantico, A., Hung, J., Menon, H. G., Spyros Darmanis, Brightbill, H. D., Garfield, D. A., & Rock, J. R. (2024). IL-4-induced SOX9 confers lineage plasticity to aged adult lung stem cells. *Cell Reports*, 43(8), 114569–114569. https://doi.org/10.1016/j.celrep.2024.114569

Camper, N., Glasgow, A. M. A., Osbourn, M., Quinn, D. J., Small, D. M., McLean, D. T., Lundy, F. T., Elborn, J. S., McNally, P., Ingram, R. J., Weldon, S., & Taggart, C. C. (2015). A secretory leukocyte protease inhibitor variant with improved activity against lung infection. *Mucosal Immunology*, 9(3), 669–676. https://doi.org/10.1038/mi.2015.90

Cao, X., Surma, M. A., & Simons, K. (2012). Polarized sorting and trafficking in epithelial cells. *Cell Research*, 22(5), 793–805. https://doi.org/10.1038/cr.2012.64

Cao, J., Spielmann, M., Qiu, X., Huang, X., Ibrahim, D. M., Hill, A. J., Zhang, F., Mundlos, S., Christiansen, L., Steemers, F. J., Trapnell, C., & Shendure, J. (2019). The single-cell transcriptional landscape of mammalian organogenesis. *Nature*, 566(7745), 496–502. https://doi.org/10.1038/s41586-019-0969-x

Choi, J., Park, J.-E., Tsagkogeorga, G., Yanagita, M., Koo, B.-K., Han, N., & Lee, J.-H. (2020). Inflammatory Signals Induce AT2 Cell-Derived Damage-Associated Transient Progenitors that Mediate Alveolar Regeneration. *Cell Stem Cell*, 27(3), 366-382.e7. https://doi.org/10.1016/j.stem.2020.06.020

Corrò, C., Novellasdemunt, L., & Li, V. S. W. (2020). A brief history of organoids. *American Journal of Physiology-Cell Physiology*, *319*(1), C151–C165. https://doi.org/10.1152/ajpcell.00120.2020

de Kleer, I. M., Kool, M., de Bruijn, M. J. W., Willart, M., van Moorleghem, J., Schuijs, M. J., Plantinga, M., Beyaert, R., Hams, E., Fallon, P. G., Hammad, H., Hendriks, R. W., & Lambrecht, B. N. (2016). Perinatal Activation of the Interleukin-33 Pathway Promotes Type 2 Immunity in the Developing Lung. *Immunity*, 45(6), 1285–1298. https://doi.org/10.1016/j.immuni.2016.10.031

Deguchi, E., Lin, S., Hirayama, D., Matsuda, K., Akira Tanave, Kenta Sumiyama, Shinya Tsukiji, Otani, T., Mikio Furuse, Sorkin, A., Matsuda, M., & Terai, K. (2024). Low-affinity ligands of the epidermal growth factor receptor are long-range signal transmitters in collective cell migration of epithelial cells. *Cell Reports*, 43(11), 114986–114986. https://doi.org/10.1016/j.celrep.2024.114986

Dong, P., Maddali, M. V., Srimani, J. K., Thélot, F., Nevins, J. R., Mathey-Prevot, B., & You, L. (2014). Division of labour between Myc and G1 cyclins in cell cycle commitment and pace control. *Nature Communications*, 5(1). https://doi.org/10.1038/ncomms5750

Eislmayr, K., Bestehorn, A., Morelli, L., Borroni, M., Walle, L. V., Lamkanfi, M., & Kovarik, P. (2022). Non-redundancy of IL-1α and IL-1β is defined by distinct regulation of tissues orchestrating resistance versus tolerance to infection. *Science Advances*, 8(9). https://doi.org/10.1126/sciadv.abj729

Enomoto, Y., Katsura, H., Fujimura, T., Ogata, A., Baba, S., Yamaoka, A., Kihara, M., Abe, T., Nishimura, O., Kadota, M., Hazama, D., Tanaka, Y., Yoshimasa Maniwa, Nagano, T., & Morimoto, M. (2023). Autocrine TGF-β-positive feedback in profibrotic AT2-lineage cells plays a crucial role in non-inflammatory lung fibrogenesis. *Nature Communications*, 14(1). https://doi.org/10.1038/s41467-023-40617-y

Franzén, O., Gan, L.-M., & Björkegren, J. L. M. (2019). PanglaoDB: a web server for exploration of mouse and human single-cell RNA sequencing data. *Database*, 2019. https://doi.org/10.1093/database/baz046

Frum, T., Hsu, P. P., Renee, Conchola, A. S., Zhang, C. J., Utter, O. R., Anand, A., Zhang, Y., Clark, S. G., Glass, I., Sexton, J. Z., & Spence, J. R. (2023). Opposing roles for TGFβ- and BMP-signaling during nascent alveolar differentiation in the developing human lung. *Npj Regenerative Medicine*, 8(1). https://doi.org/10.1038/s41536-023-00325-z

Ghonim, M. A., Boyd, D. F., Flerlage, T., & Thomas, P. G. (2023). Pulmonary inflammation and fibroblast immunoregulation: from bench to bedside. *Journal of Clinical Investigation*, 133(17). https://doi.org/10.1172/jci170499

Giri, J., Das, R., Nylen, E., Chinnadurai, R., & Galipeau, J. (2020). CCL2 and CXCL12 Derived from Mesenchymal Stromal Cells Cooperatively Polarize IL-10+ Tissue Macrophages to Mitigate Gut Injury. *Cell Reports*, 30(6), 1923-1934.e4. https://doi.org/10.1016/j.celrep.2020.01.047

Goltsis, O., Bilodeau, C., Wang, J., Luo, D., Asgari, M., Bozec, L., Pettersson, A., Leibel, S. L., & Post, M. (2024). Influence of mesenchymal and biophysical components

on distal lung organoid differentiation. *Stem Cell Research & Therapy*, 15(1), 273. https://doi.org/10.1186/s13287-024-03890-2

Goodwin, A. T., John, A. E., Joseph, C., Habgood, A., Tatler, A. L., Katalin Susztak, Palmer, M., Offermanns, S., Henderson, N. C., & Jenkins, R. G. (2023). Stretch regulates alveologenesis and homeostasis via mesenchymal Gαq/11-mediated TGFβ2 activation. *Development*, 150(9). https://doi.org/10.1242/dev.201046

Guan, T., Zhou, X., Zhou, W., & Lin, H. (2023). Regulatory T cell and macrophage crosstalk in acute lung injury: future perspectives. *Cell Death Discovery*, 9(1). https://doi.org/10.1038/s41420-023-01310-7

Ha Na Seo, Jeong, H., Hyung Joon Joo, Seung Hong Choi, Park, C.-Y., Kim, J.-H., Ji Yeob Choi, Cui, L.-H., Soon Hyung Hong, Chung, S., & Do Sun Lim. (2016). Intrinsic FGF2 and FGF5 promotes angiogenesis of human aortic endothelial cells in 3D microfluidic angiogenesis system. *Scientific Reports*, 6(1). https://doi.org/10.1038/srep28832

Hewitt, R. J., & Lloyd, C. M. (2021). Regulation of immune responses by the airway epithelial cell landscape. *Nature Reviews Immunology*, 21, 347–362. https://doi.org/10.1038/s41577-020-00477-9

Hollingsworth, J. W., Li, Z., Brass, D. M., Stavros Garantziotis, Timberlake, S. H., Kim, A., Hossain, I., Savani, R. C., & Schwartz, D. A. (2007). CD44 Regulates Macrophage Recruitment to the Lung in Lipopolysaccharide-Induced Airway Disease. *American Journal of Respiratory Cell and Molecular Biology*, 37(2), 248–253. https://doi.org/10.1165/rcmb.2006-0363oc

Holtzman, M. J., Morton, J. D., Shornick, L. P., Tyner, J. W., O'Sullivan, M. P., Antao, A., Lo, M., Castro, M., & Walter, M. J. (2002). Immunity, Inflammation, and Remodeling in the Airway Epithelial Barrier: Epithelial-Viral-Allergic Paradigm. *Physiological Reviews*, 82(1), 19–46. https://doi.org/10.1152/physrev.00020.2001

Itsaso Garcia-Arcos, Park, S. S., Mai, M., Alvarez-Buve, R., Chow, L., Cai, H., Baumlin-Schmid, N., Agudelo, C. W., Martinez, J., Kim, M. D., Dabo, A. J., Salathe, M., Goldberg, I. J., & Foronjy, R. F. (2022). LRP1 loss in airway epithelium exacerbates smoke-induced oxidative damage and airway remodeling. *Journal of Lipid Research*, 63(4), 100185–100185. https://doi.org/10.1016/j.jlr.2022.100185

Jones, D. L., Morley, M. P., Li, X., Ying, Y., Zhao, G., Schaefer, S. E., Rodriguez, L. R., Cardenas-Diaz, F. L., Li, S., Zhou, S., Chembazhi, U. V., Kim, M., Shen, C., Nottingham, A., Lin, S. M., Cantu, E., Diamond, J. M., Basil, M. C., Vaughan, A. E., & Morrisey, E. E. (2024). An injury-induced mesenchymal-epithelial cell niche coordinates regenerative responses in the lung. *Science*, 386(6727). https://doi.org/10.1126/science.ado5561

Joshi, R., Heinz, A., Fan, Q., Guo, S., Monia, B., Schmelzer, C. E. H., Weiss, A. S., Batie, M., Parameshwaran, H., & Varisco, B. M. (2018). Role forCela1in Postnatal Lung Remodeling and Alpha-1 Antitrypsin–Deficient Emphysema. *American Journal of Respiratory Cell and Molecular Biology*, 59(2), 167–178. https://doi.org/10.1165/rcmb.2017-0361oc

Kadur Lakshminarasimha Murthy, P., Sontake, V., Tata, A., Kobayashi, Y., Macadlo, L., Okuda, K., Conchola, A. S., Nakano, S., Gregory, S., Miller, L. A., Spence, J. R., Engelhardt, J. F., Boucher, R. C., Rock, J. R., Randell, S. H., & Tata, P. R. (2022). Human distal lung maps and lineage hierarchies reveal a bipotent progenitor. *Nature*, 604(7904), 111–119. https://doi.org/10.1038/s41586-022-04541-3

Katsura, H., Kobayashi, Y., Tata, P. R., & Hogan, B. L. M. (2019). IL-1 and TNFα Contribute to the Inflammatory Niche to Enhance Alveolar Regeneration. *Stem Cell Reports*, 12(4), 657–666. https://doi.org/10.1016/j.stemcr.2019.02.013

Keerthi Raja, M. R., Gupta, G., Atkinson, G., Kathrein, K., Armstrong, A., Gower, M., Roninson, I., Broude, E., Chen, M., Ji, H., Lim, C., Wang, H., Fan, D., Xu, P., Li, J., Zhou, G., & Chen, H. (2024). Host-derived Interleukin 1α induces an immunosuppressive tumor microenvironment via regulating monocyte-to-macrophage differentiation. *BioRxiv*. https://doi.org/10.1101/2024.05.03.592354

Kim, C. F. B., Jackson, E. L., Woolfenden, A. E., Lawrence, S., Babar, I., Vogel, S., Crowley, D., Bronson, R. T., & Jacks, T. (2005). Identification of Bronchioalveolar Stem Cells in Normal Lung and Lung Cancer. *Cell*, 121(6), 823–835. https://doi.org/10.1016/j.cell.2005.03.032

Königshoff, M., & Eickelberg, O. (2010). WNT Signaling in Lung Disease. *American Journal of Respiratory Cell and Molecular Biology*, 42(1), 21–31. https://doi.org/10.1165/rcmb.2008-0485tr

Lewis, A. E., Kuwahara, A., Franzosi, J., & Bush, J. O. (2022). Tracheal separation is driven by NKX2-1-mediated repression of Efnb2 and regulation of endodermal cell sorting. *Cell Reports*, 38(11), 110510–110510. https://doi.org/10.1016/j.celrep.2022.110510

Liberzon, A., Birger, C., Thorvaldsdóttir, H., Ghandi, M., Mesirov, Jill P., & Tamayo, P. (2015). The Molecular Signatures Database Hallmark Gene Set Collection. *Cell Systems*, 1(6), 417–425. https://doi.org/10.1016/j.cels.2015.12.004

Lin, B., Shah, V. S., Chernoff, C., Sun, J., Shipkovenska, G. G., Vladimir Vinarsky, Avinash Waghray, Xu, J., Leduc, A. D., Hintschich, C. A., Manalee Vishnu Surve, Xu, Y., Capen, D. E., Villoria, J., Dou, Z., Hariri, L. P., & Rajagopal, J. (2024). Airway hillocks are injury-resistant reservoirs of unique plastic stem cells. *Nature*, 629(8013), 869–877. https://doi.org/10.1038/s41586-024-07377-1

Liu, C., Zheng, S., Lu, Z., Wang, Z., Wang, S., Feng, X., Wang, Y., Sun, N., & He, J. (2022). S100A7 attenuates immunotherapy by enhancing immunosuppressive tumor microenvironment in lung squamous cell carcinoma. *Signal Transduction and Targeted Therapy*, 7(1). https://doi.org/10.1038/s41392-022-01196-4

Liu, F., Lagares, D., Choi, K. M., Stopfer, L., Marinković, A., Vrbanac, V., Probst, C. K., Hiemer, S. E., Sisson, T. H., Horowitz, J. C., Rosas, I. O., Fredenburgh, L. E., Feghali-Bostwick, C., Varelas, X., Tager, A. M., & Tschumperlin, D. J. (2015). Mechanosignaling through YAP and TAZ drives fibroblast activation and fibrosis. *American Journal of Physiology - Lung Cellular and Molecular Physiology*, 308(4), L344–L357. https://doi.org/10.1152/ajplung.00300.2014

Liu, M. Y., Chen, B., Mehdi Borji, Garcia, C., Dost, M., Moye, A. L., Abdulla, N. M., Paschini, M., Rollins, S. D., Wang, R., Schnapp, L. M., Khalil, H. A., Wu, C. J., Sharma, N. S., & Kim, C. F. (2024). Human Airway and Alveolar Organoids from BAL Fluid. *American Journal of Respiratory and Critical Care Medicine*, 209(12), 1501–1504. https://doi.org/10.1164/rccm.202310-1831le

Liu, T., Laidlaw, T. M., Feng, C., Xing, W., Shen, S., Milne, G. L., & Boyce, J. A. (2012). Prostaglandin E2 deficiency uncovers a dominant role for thromboxane A2 in house dust mite-induced allergic pulmonary inflammation. *Proceedings of the National Academy of Sciences*, 109(31), 12692–12697. https://doi.org/10.1073/pnas.1207816109

Luecken, M. D., & Theis, F. J. (2019). Current best practices in single-cell RNA-seq analysis: a tutorial. *Molecular Systems Biology*, 15(6). https://doi.org/10.15252/msb.20188746

Manneken, J. D., & Currie, P. D. (2023). Macrophage-stem cell crosstalk: regulation of the stem cell niche. *Development*, 150(8). https://doi.org/10.1242/dev.201510

Martins, L. R., Sieverling, L., Michelhans, M., Schiller, C., Erkut, C., Grünewald, T. G. P., Triana, S., Fröhling, S., Velten, L., Glimm, H., & Scholl, C. (2024). Single-cell division tracing and transcriptomics reveal cell types and differentiation paths in the regenerating lung. *Nature Communications*, 15(1). https://doi.org/10.1038/s41467-024-46469-4

Matkovic Leko, I., Schneider, R. T., Thimraj, T. A., Schrode, N., Beitler, D., Liu, H.-Y., Beaumont, K., Chen, Y.-W., & Snoeck, H.-W. (2023). A distal lung organoid model to study interstitial lung disease, viral infection, and human lung development. *Nature Protocols*, 18(7), 2283–2312. https://doi.org/10.1038/s41596-023-00827-6

Medzhitov, R. (2021). The spectrum of inflammatory responses. *Science*, 374(6571), 1070–1075. https://doi.org/10.1126/science.abi5200

Micochova, P., Zhao, N., Shabana, O., Fischer, R., & Gupta, R. K. (2024). CD4 T cell contact drives macrophage cell cycle G0-G1 transition. *Signal Transduction and Targeted Therapy*, 9(1). https://doi.org/10.1038/s41392-024-02053-2

Mo, Y., Kang, H., Bang, J.-Y., Shin, J. W., Kim, H. Y., Cho, S.-H., & Kang, H.-R. (2022). Intratracheal administration of mesenchymal stem cells modulates lung macrophage polarization and exerts anti-asthmatic effects. *Scientific Reports*, 12(1). https://doi.org/10.1038/s41598-022-14846-y

Montoro, D. T., Haber, A. L., Biton, M., Vinarsky, V., Lin, B., Birket, S. E., Yuan, F., Chen, S., Leung, H. M., Villoria, J., Rogel, N., Burgin, G., Tsankov, A. M., Waghray, A., Slyper, M., Waldman, J., Nguyen, L., Dionne, D., Rozenblatt-Rosen, O., & Tata, P. R. (2018). A revised airway epithelial hierarchy includes CFTR-expressing Ionocytes. *Nature*, 560(7718), 319–324. https://doi.org/10.1038/s41586-018-0393-7

Morrison, T. J., Jackson, M. V., Cunningham, E. K., Kissenpfennig, A., McAuley, D. F., O'Kane, C. M., & Krasnodembskaya, A. D. (2017). Mesenchymal Stromal Cells Modulate Macrophages in Clinically Relevant Lung Injury Models by Extracellular Vesicle Mitochondrial Transfer. *American Journal of Respiratory and Critical Care Medicine*, 196(10), 1275–1286. https://doi.org/10.1164/rccm.201701-0170oc

Morrow, J. D., Yun, J. H., & Hersh, C. P. (2024). Lung Single-Cell Transcriptomics in Alpha-1 Antitrypsin Deficiency. *American Journal of Respiratory Cell and Molecular Biology*, 71(2), 254–256. https://doi.org/10.1165/rcmb.2024-0064le

Murrow, L. M., Weber, R. J., & Gartner, Z. J. (2017). Dissecting the stem cell niche with organoid models: an engineering-based approach. *Development* (Cambridge, England), 144(6), 998–1007. https://doi.org/10.1242/dev.140905

Nalio Ramos, R., Missolo-Koussou, Y., Gerber-Ferder, Y., Bromley, C. P., Bugatti, M., Núñez, N. G., Tosello Boari, J., Richer, W., Menger, L., Denizeau, J., Sedlik, C., Caudana, P., Kotsias, F., Niborski, L. L., Viel, S., Bohec, M., Lameiras, S., Baulande, S., Lesage, L., & Nicolas, A. (2022). Tissue-resident FOLR2+ macrophages associate with CD8+ T cell infiltration in human breast cancer. *Cell*, 185(7), 1189-1207.e25. https://doi.org/10.1016/j.cell.2022.02.021

Nardell, E. A., & Brody, J. S. (1982). Determinants of mechanical properties of rat lung during postnatal development. *Journal of Applied Physiology*, 53(1), 140–148. https://doi.org/10.1152/jappl.1982.53.1.140

Negretti, N. M., Son, Y., Crooke, P., Plosa, E. J., Benjamin, J. T., Jetter, C. S., Bunn, C., Mignemi, N., Marini, J., Hackett, A. N., Ransom, M., Garg, S., Nichols, D., Guttentag, S. H., Pua, H. H., Blackwell, T. S., Zacharias, W., Frank, D. B., Kozub, J. A., & Mahadevan-Jansen, A. (2025). Epithelial outgrowth through

mesenchymal rings drives alveologenesis. *JCI Insight*. https://doi.org/10.1172/jci.insight.187876

Neri, T., Armani, C., Pergola, A., Cordazzo, C., Carmazzi, Y., Brunelleschi, S., Bardelli, C., Breschi, M., Paggiaro, P. L., & Celi, A. (2010). Role of NF- B and PPAR- in lung inflammation induced by monocyte-derived microparticles. *The European Respiratory Journal*, 37(6), 1494–1502. https://doi.org/10.1183/09031936.00023310

Nichane, M., Javed, A., Sivakamasundari, V., Ganesan, M., Ang, L. T., Kraus, P., Lufkin, T., Loh, K. M., & Lim, B. (2017). Isolation and 3D expansion of multipotent Sox9+ mouse lung progenitors. *Nature Methods*, 14(12), 1205–1212. https://doi.org/10.1038/nmeth.4498

Niethamer, T. K., Planer, J. D., Morley, M. P., Babu, A., Zhao, G., Basil, M. C., Cantu, E., Frank, D. B., Diamond, J. M., Nottingham, A. N., Li, S., Sharma, A., Hallquist, H., Levin, L. I., Zhou, S., Vaughan, A. E., & Morrisey, E. E. (2025). Longitudinal single-cell profiles of lung regeneration after viral infection reveal persistent injury-associated cell states. *Cell Stem Cell*, 32(2). https://doi.org/10.1016/j.stem.2024.12.002

Nikolić, M. Z., & Rawlins, E. L. (2017). Lung Organoids and Their Use to Study Cell-Cell Interaction. *Current Pathobiology Reports*, 5(2), 223–231. https://doi.org/10.1007/s40139-017-0137-7

Nolte, R. T., Wisely, G. B., Westin, S., Cobb, J. E., Lambert, M. H., Kurokawa, R., Rosenfeld, M. G., Willson, T. M., Glass, C. K., & Milburn, M. V. (1998). Ligand binding and co-activator assembly of the peroxisome proliferator-activated receptor-γ. *Nature*, 395(6698), 137–143. https://doi.org/10.1038/25931

Nwokoye, P. N., & Abilez, O. J. (2024). Bioengineering methods for vascularizing organoids. *Cell Reports Methods*, *4*(6), 100779. https://doi.org/10.1016/j.crmeth.2024.100779

O'Reilly, M., & Thébaud, B. (2014). Animal models of bronchopulmonary dysplasia. The term rat models. *American Journal of Physiology-Lung Cellular and Molecular Physiology*, 307(12), L948–L958. https://doi.org/10.1152/ajplung.00160.2014

Ostrin, E. J., Little, D. R., Gerner-Mauro, K. N., Sumner, E. A., Ríos-Corzo, R., Ambrosio, E., Holt, S. E., Forcioli-Conti, N., Akiyama, H., Hanash, S. M., Kimura, S., Huang, S. X. L., & Chen, J. (2018). β-Catenin maintains lung epithelial progenitors after lung specification. *Development* (Cambridge, England), 145(5), dev160788. https://doi.org/10.1242/dev.160788

Palmieri, E. M., Gonzalez-Cotto, M., Baseler, W. A., Davies, L. C., Ghesquière, B., Maio, N., Rice, C. M., Rouault, T. A., Cassel, T., Higashi, R. M., Lane, A. N., Fan, T. W.-

M. ., Wink, D. A., & McVicar, D. W. (2020). Nitric oxide orchestrates metabolic rewiring in M1 macrophages by targeting aconitase 2 and pyruvate dehydrogenase. *Nature Communications*, 11(1), 698. https://doi.org/10.1038/s41467-020-14433-7

Panza, P., Kim, H.-T., Lautenschläger, T., Piesker, J., Günther, S., Alayoubi, Y., Cleaver, O., Looso, M., & Stainier, D. (2025). The lung microvasculature promotes alveolar type 2 cell differentiation via secreted SPARCL1. *Stem Cell Reports*, 20(4), 102451–102451. https://doi.org/10.1016/j.stemcr.2025.102451

Patel, D. F., Peiró, T., Shoemark, A., Samia Akthar, Walker, S. A., Grabiec, A. M., Jackson, P. L., Hussell, T., Amit Gaggar, Xu, X., Trevor, J. L., Li, J., Steele, C., Tavernier, G., Blalock, J. E., Niven, R. M., Gregory, L. G., Simpson, A., Lloyd, C. M., & Snelgrove, R. J. (2018). An extracellular matrix fragment drives epithelial remodeling and airway hyperresponsiveness. *Science Translational Medicine*, 10(455). https://doi.org/10.1126/scitranslmed.aaq0693

Planer, J. D., & Morrisey, E. E. (2022). After the Storm: Regeneration, Repair, and Reestablishment of Homeostasis Between the Alveolar Epithelium and Innate Immune System Following Viral Lung Injury. *Annual Review of Pathology: Mechanisms of Disease*, 18(1). https://doi.org/10.1146/annurev-pathmechdis-031621-024344

Radomir, L., Kramer, M. P., Perpinial, M., Schottlender, N., Rabani, S., David, K., Wiener, A., Lewinsky, H., Becker-Herman, S., Aharoni, R., Milo, R., Mauri, C., & Shachar, I. (2021). The survival and function of IL-10-producing regulatory B cells are negatively controlled by SLAMF5. *Nature Communications*, 12(1). https://doi.org/10.1038/s41467-021-22230-z

Raredon, M. S. B., Yang, J., Garritano, J., Wang, M., Kushnir, D., Schupp, J. C., Adams, T. S., Greaney, A. M., Leiby, K. L., Kaminski, N., Kluger, Y., Levchenko, A., & Niklason, L. E. (2022). Computation and visualization of cell–cell signaling topologies in single-cell systems data using Connectome. *Scientific Reports*, 12(1). https://doi.org/10.1038/s41598-022-07959-x

Raredon, M.S., Yang, J., Kothapalli, N., Lewis, W., Kaminski, N., Niklason, L. E., & Kluger, Y. (2023). Comprehensive visualization of cell–cell interactions in single-cell and spatial transcriptomics with NICHES. *Bioinformatics*, 39(1). https://doi.org/10.1093/bioinformatics/btac775

Sachs, N., Papaspyropoulos, A., Zomer-van Ommen, D. D., Heo, I., Böttinger, L., Klay, D., Weeber, F., Huelsz-Prince, G., Iakobachvili, N., Amatngalim, G. D., de Ligt, J., van Hoeck, A., Proost, N., Viveen, M. C., Lyubimova, A., Teeven, L., Derakhshan, S., Korving, J., Begthel, H., & Dekkers, J. F. (2019). Long-term expanding human airway organoids for disease modeling. *The EMBO Journal*, 38(4). https://doi.org/10.15252/embj.2018100300

Salwig, I., Spitznagel, B., Vazquez-Armendariz, A. I., Khalooghi, K., Guenther, S., Herold, S., Szibor, M., & Braun, T. (2019). Bronchioalveolar stem cells are a main source for regeneration of distal lung epithelia in vivo. *The EMBO Journal*, 38(12). https://doi.org/10.15252/embj.2019102099

Sanchez-Esteban, J., Cicchiello, L. A., Wang, Y., Tsai, S.-W., Williams, L. K., Torday, J. S., & Rubin, L. P. (2001). Mechanical stretch promotes alveolar epithelial type II cell differentiation. *Journal of Applied Physiology* (1985, Online), 91(2), 589–595. https://doi.org/10.1152/jappl.2001.91.2.589

Shao, X., Taha, I. N., Clauser, K. R., Gao, Y. (Tom), & Naba, A. (2019). MatrisomeDB: the ECM-protein knowledge database. *Nucleic Acids Research*, 48(D1), D1136–D1144. https://doi.org/10.1093/nar/gkz849

Shen, W.-K., Chen, S.-Y., Gan, Z.-Q., Zhang, Y.-Z., Yue, T., Chen, M.-M., Xue, Y., Hu, H., & Guo, A.-Y. (2022). AnimalTFDB 4.0: a comprehensive animal transcription factor database updated with variation and expression annotations. *Nucleic Acids Research*, 51(D1), D39–D45. https://doi.org/10.1093/nar/gkac907

Shiraishi, K., Shah, P. P., Morley, M. P., Loebel, C., Santini, G. T., Katzen, J., Basil, M. C., Lin, S. M., Planer, J. D., Cantu, E., Jones, D. L., Nottingham, A. N., Li, S., Cardenas-Diaz, F. L., Zhou, S., Burdick, J. A., Jain, R., & Morrisey, E. E. (2023). Biophysical forces mediated by respiration maintain lung alveolar epithelial cell fate. *Cell*, 0(0). https://doi.org/10.1016/j.cell.2023.02.010

Sintes, J., Romero, X., de Salort, J., Terhorst, C., & Engel, P. (2010). Mouse CD84 is a pan-leukocyte cell-surface molecule that modulates LPS-induced cytokine secretion by macrophages. *Journal of Leukocyte Biology*, 88(4), 687–697. https://doi.org/10.1189/jlb.1109756

Ståhl, S., Kaminskyy, V. O., Efazat, G., Hyrslova Vaculova, A., Rodriguez-Nieto, S., Moshfegh, A., Lewensohn, R., Viktorsson, K., & Zhivotovsky, B. (2013). Inhibition of Ephrin B3-mediated survival signaling contributes to increased cell death response of non-small cell lung carcinoma cells after combined treatment with ionizing radiation and PKC 412. *Cell Death & Disease*, 4(1), e454–e454. https://doi.org/10.1038/cddis.2012.188

Stouch, A. N., McCoy, A. M., Greer, R. M., Lakhdari, O., Yull, F. E., Blackwell, T. S., Hoffman, H. M., & Prince, L. S. (2016). IL-1β and Inflammasome Activity Link Inflammation to Abnormal Fetal Airway Development. *Journal of Immunology* (Baltimore, Md.: 1950), 196(8), 3411–3420. https://doi.org/10.4049/jimmunol.1500906

Street, K., Risso, D., Fletcher, R. B., Das, D., Ngai, J., Yosef, N., Purdom, E., & Dudoit, S. (2018). Slingshot: cell lineage and pseudotime inference for single-cell

transcriptomics. *BMC Genomics*, 19(1). https://doi.org/10.1186/s12864-018-4772-0

Strunz, M., Simon, L. M., Ansari, M., Kathiriya, J. J., Angelidis, I., Mayr, C. H., Tsidiridis, G., Lange, M., Mattner, L. F., Yee, M., Ogar, P., Sengupta, A., Kukhtevich, I., Schneider, R., Zhao, Z., Voss, C., Stoeger, T., Neumann, J. H. L., Hilgendorff, A., & Behr, J. (2020). Alveolar regeneration through a Krt8+ transitional stem cell state that persists in human lung fibrosis. *Nature Communications*, 11(1). https://doi.org/10.1038/s41467-020-17358-3

Suwara, M. I., Green, N. J., Borthwick, L. A., Mann, J., Mayer-Barber, K. D., Barron, L., Corris, P. A., Farrow, S. N., Wynn, T. A., Fisher, A. J., & Mann, D. A. (2013). IL-1α released from damaged epithelial cells is sufficient and essential to trigger inflammatory responses in human lung fibroblasts. *Mucosal Immunology*, 7(3), 684–693. https://doi.org/10.1038/mi.2013.87

Tata, P. R., & Rajagopal, J. (2017). Plasticity in the lung: making and breaking cell identity. *Development*, 144(5), 755–766. https://doi.org/10.1242/dev.143784

Van den Berge, K., Roux de Bézieux, H., Street, K., Saelens, W., Cannoodt, R., Saeys, Y., Dudoit, S., & Clement, L. (2020). Trajectory-based differential expression analysis for single-cell sequencing data. *Nature Communications*, 11(1), 1–13. https://doi.org/10.1038/s41467-020-14766-3

Vining, K. H., & Mooney, D. J. (2017). Mechanical forces direct stem cell behavior in development and regeneration. *Nature Reviews Molecular Cell Biology*, 18(12), 728–742. https://doi.org/10.1038/nrm.2017.108

Walker, J. L., Bleaken, B. M., Romisher, A. R., Alnwibit, A. A., & Menko, A. S. (2018). In wound repair, vimentin mediates the transition of mesenchymal leader cells to a myofibroblast phenotype. *Molecular Biology of the Cell*, 29(13), 1555–1570. https://doi.org/10.1091/mbc.e17-06-0364

Wang, C., Yu, Q., Song, T., Wang, Z., Song, L., Yang, Y., Shao, J., Li, J., Ni, Y., Chao, N.-N., Zhang, L., & Wei Min Li. (2022). The heterogeneous immune landscape between lung adenocarcinoma and squamous carcinoma revealed by single-cell RNA sequencing. *Signal Transduction and Targeted Therapy*, 7(1). https://doi.org/10.1038/s41392-022-01130-8

Wang, H., Hosakote, Y. M., Boor, P. J., Yang, J., Zhang, Y., Yu, X., Gonzales, C., Levine, C. B., McLellan, S., Cloutier, N., Xie, X., Shi, P.-Y., Ren, P., Hu, H., Sun, K., Soong, L., Sun, J., & Liang, Y. (2024). The alarmin IL-33 exacerbates pulmonary inflammation and immune dysfunction in SARS-CoV-2 infection. *iScience*, 27(6), 110117–110117. https://doi.org/10.1016/j.isci.2024.110117

Warburton, D., Schwarz, M., Tefft, D., Flores-Delgado, G., Anderson, K. D., & Cardoso, W. V. (2000). The molecular basis of lung morphogenesis. *Mechanisms of Development*, 92(1), 55–81. https://doi.org/10.1016/s0925-4773(99)00325-1

Warren, R., Klinkhammer, K., Lyu, H., Knopp, J., Yuan, T., Yao, C., Stripp, B., & De Langhe, S. P. (2024). Cell competition drives bronchiolization and pulmonary fibrosis. *Nature Communications*, 15(1). https://doi.org/10.1038/s41467-024-54997-2

Willart, M. A. M., Deswarte, K., Pouliot, P., Braun, H., Beyaert, R., Lambrecht, B. N., & Hammad, H. (2012). Interleukin-1α controls allergic sensitization to inhaled house dust mite via the epithelial release of GM-CSF and IL-33. *Journal of Experimental Medicine*, 209(8), 1505–1517. https://doi.org/10.1084/jem.20112691

Wörsdörfer, P., Dalda, N., Kern, A., Krüger, S., Wagner, N., Kwok, C. K., Henke, E., & Ergün, S. (2019). Generation of complex human organoid models including vascular networks by incorporation of mesodermal progenitor cells. *Scientific Reports*, 9(1). https://doi.org/10.1038/s41598-019-52204-7

Wu, T., Hu, E., Xu, S., Chen, M., Guo, P., Dai, Z., Feng, T., Zhou, L., Tang, W., Zhan, L., Fu, X., Liu, S., Bo, X., & Yu, G. (2021). clusterProfiler 4.0: A universal enrichment tool for interpreting omics data. *The Innovation*, 2(3), 100141.

Xu, B., Chen, C., Chen, H., Zheng, S.-G., Bringas, P., Xu, M., Zhou, X., Chen, D., Umans, L., Zwijsen, A., & Shi, W. (2011). Smad1 and its target gene Wif1 coordinate BMP and Wnt signaling activities to regulate fetal lung development. *Development*, 138(5), 925–935. https://doi.org/10.1242/dev.062687

Zepp, J. A., Zacharias, W. J., Frank, D. B., Cavanaugh, C. A., Zhou, S., Morley, M. P., & Morrisey, E. E. (2017). Distinct Mesenchymal Lineages and Niches Promote Epithelial Self-Renewal and Myofibrogenesis in the Lung. *Cell*, 170(6), 1134-1148.e10. https://doi.org/10.1016/j.cell.2017.07.034

Zhang, H., C. Kimberly Tsui, Garcia, G., Joe, L. K., Wu, H., Ayane Maruichi, Fan, W., Sentibel Pandovski, Yoon, P. H., Webster, B. M., Durieux, J., Frankino, P. A., Ryo Higuchi-Sanabria, & Dillin, A. (2024). The extracellular matrix integrates mitochondrial homeostasis. *Cell*, 187(16). https://doi.org/10.1016/j.cell.2024.05.057

Zhang, S., Zhang, L., Wang, L., Wang, H., Wu, J., Cai, H., Mo, C., & Yang, J. (2023). Machine learning identified MDK score has prognostic value for idiopathic pulmonary fibrosis based on integrated bulk and single cell expression data. *Frontiers in Genetics*, 14(23). https://doi.org/10.3389/fgene.2023.1246983

Zhang, Y., Black, K. E., Phung, T.-K. N., Sujatha Rajeev Thundivalappil, Lin, T., Wang, W., Xu, J., Zhang, C., Hariri, L. P., Lapey, A., Li, H., Lerou, P. H., Ai, X., Que, J., Park, J.-A., Hurley, B. P., & Mou, H. (2023). Human Airway Basal Cells Undergo Reversible Squamous Differentiation and Reshape Innate Immunity. *American Journal of Respiratory Cell and Molecular Biology*, 68(6), 664–678. https://doi.org/10.1165/rcmb.2022-0299oc

Zheng, L., Zhou, Z., Lin, L., Alber, S., Watkins, S., Kaminski, N., Choi, A., & Morse, D. (2008). Carbon Monoxide Modulates α–Smooth Muscle Actin and Small Proline Rich-1a Expression in Fibrosis. *American Journal of Respiratory Cell and Molecular Biology*, 41(1), 85–92. https://doi.org/10.1165/rcmb.2007-0401oc

Zhou, C., Gao, Y., Ding, P., Wu, T., & Ji, G. (2023). The role of CXCL family members in different diseases. *Cell Death Discovery*, 9(1). https://doi.org/10.1038/s41420-023-01524-9

Zimmermann, N., Doepker, M. P., Witte, D. P., Stringer, K. F., Fulkerson, P. C., Pope, S. M., Brandt, E. B., Mishra, A., King, N. E., Nikolaidis, N. M., Wills-Karp, M., Finkelman, F. D., & Rothenberg, M. E. (2005). Expression and Regulation of Small Proline-Rich Protein 2 in Allergic Inflammation. *American Journal of Respiratory Cell and Molecular Biology*, 32(5), 428–435. https://doi.org/10.1165/rcmb.2004-0269oc

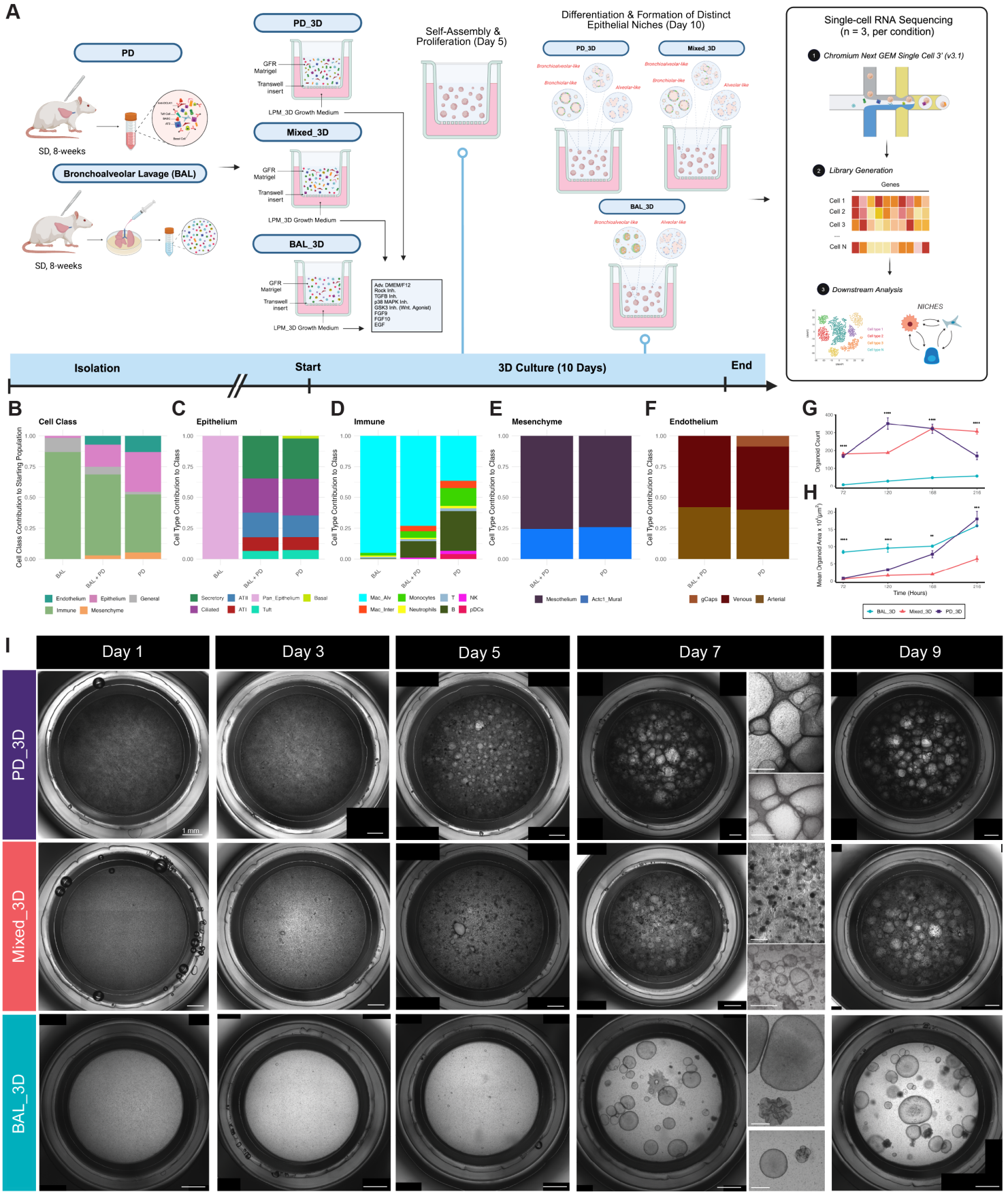

Figure 1. A tunable 3D lung organoid system enables controlled modeling of epithelial–immune–mesenchymal interactions. **A)** Schematic overview of experimental design. Cells were isolated from rat lungs via either pulmonary dissociation (PD) or bronchoalveolar lavage (BAL) at 8 weeks of age, then combined to generate three experimental groups: PD_3D (native lung dissociation), BAL_3D (immune-enriched), and Mixed_3D (1:1 mixture of PD and BAL cells). Organoids were maintained in LPM-3D progenitor medium through Day 10. Organoids were harvested for single-cell RNA sequencing (10x Genomics Chromium, n = 3 replicates per condition) and processed for downstream transcriptomic and ligand–receptor signaling analysis (NICHES). **B–F)** Quantification of major cell class distributions across conditions using scRNA-seq data. Bar graphs show proportions of: **B)** major cell lineages, including a "General" category representing cycling cells that could not be definitively assigned to a single lineage; **C)** epithelial subsets, **D)** immune subsets, **E)** mesenchymal populations, and **F)** endothelial cells. **G–H)** Quantification of morphological metrics from 3D organoid cultures over time. Organoid number **(G)** and mean organoid area **(H)** were quantified using QuPath on stitched brightfield images (n = 3 wells per condition per timepoint) (*see Methods*). ***, $p \leq 0.001$; *, $p \leq 0.01$; $p \leq 0.05$; ns, not significant; statistical comparisons performed using Welch's t-tests with Benjamini–Hochberg correction for multiple comparisons. **I)** Brightfield images of 3D organoid cultures across time (Days 1, 3, 5, 7, 9). Representative wells are shown for each condition. Insets on Day 7 show zoomed views of organoid morphology. Scale bars, 1 mm (main panels) and 200 µm (insets).

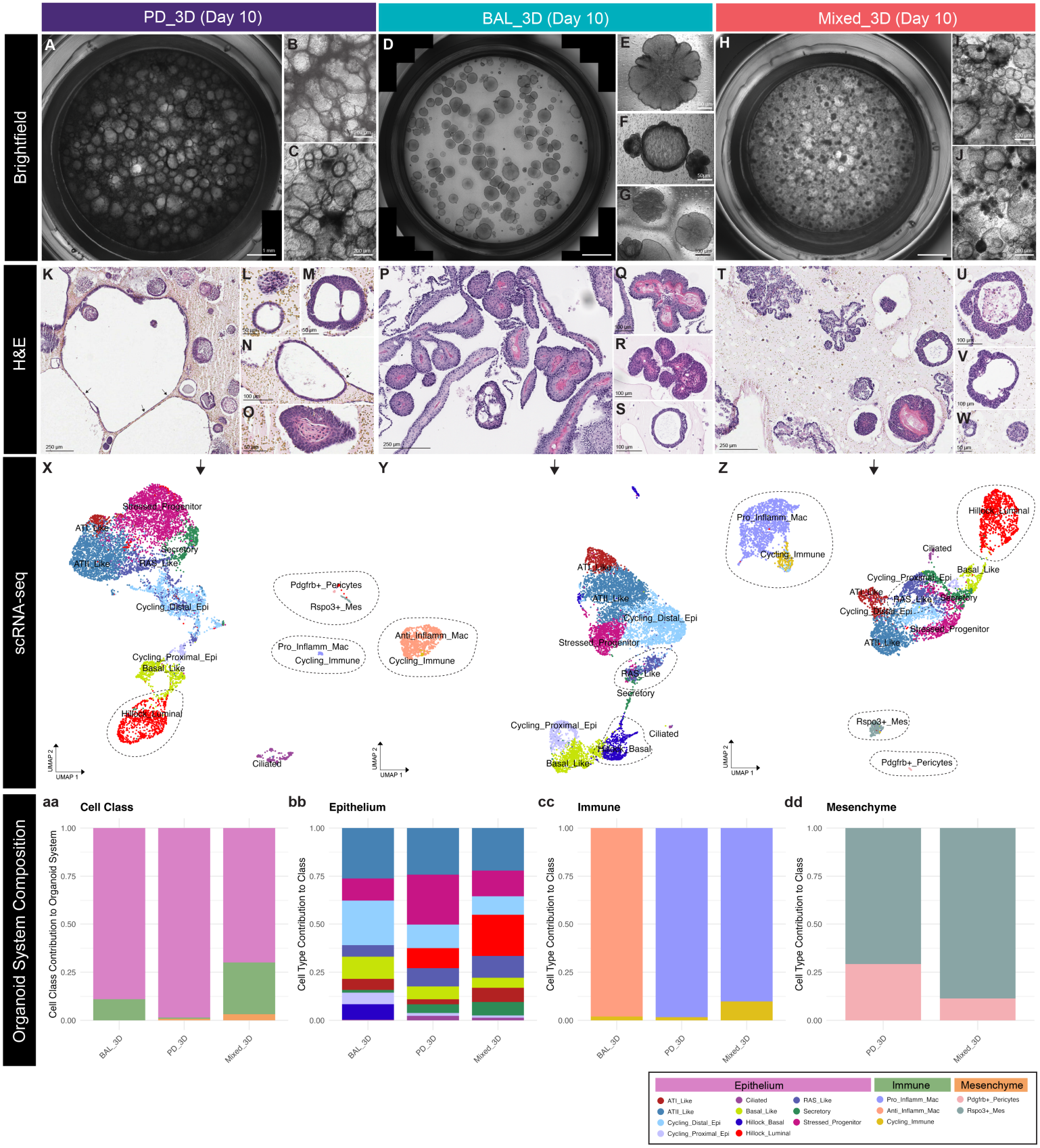

Figure 2. Day 10 organoid systems exhibit condition-specific morphologies, epithelial architectures, and cellular compositions. **A–C, D–F, H–J)** Brightfield images of representative organoid cultures on Day 10 for PD_3D **(A–C)**, BAL_3D **(D–F)**, and Mixed_3D **(H–J)**. Panels A, D, and H show stitched whole-well images (scale bar, 1mm); insets show zoomed organoids highlighting distinct morphologies across conditions (scale bars provided on individual images due to variation). **K–M**, **N–O**; **P–R**, **S**; **T–V**, **W**) Hematoxylin and eosin (H&E) staining reveals condition-specific epithelial architectures, including variations in epithelial layering, lumen formation, and structural complexity. Scale bars are shown on each image. Arrows in K and N highlight thin, flattened epithelial cells morphologically consistent with alveolar type I (ATI)-like cells. **X–Z)** UMAP projections of condition-level single-cell RNA-seq data for PD_3D **(X)**, BAL_3D **(Y)**, and Mixed_3D **(Z)**, with cells colored by annotated identity (*see legend in figure*). Circled populations mark epithelial, immune, and mesenchymal subtypes of relevance, including Hillock cells, secretory-alveolar intermediates (AT0/RAS), polarized macrophages, Rspo3+ mesenchyme, and Pdgfrb+ pericytes. Embeddings shown using node-aligned global object cell type annotations mapped back onto the condition level embeddings. **aa–dd)** Within-class breakdowns of cell type composition across conditions on day 10. Stacked bar plots show the relative proportions of specific cell types within each major class—cell classes **(aa)**, epithelial subsets **(bb)**, immune subsets **(cc)**, and mesenchymal populations **(dd)**—normalized to 1 within each class per condition. PD_3D and Mixed_3D cultures maintained.

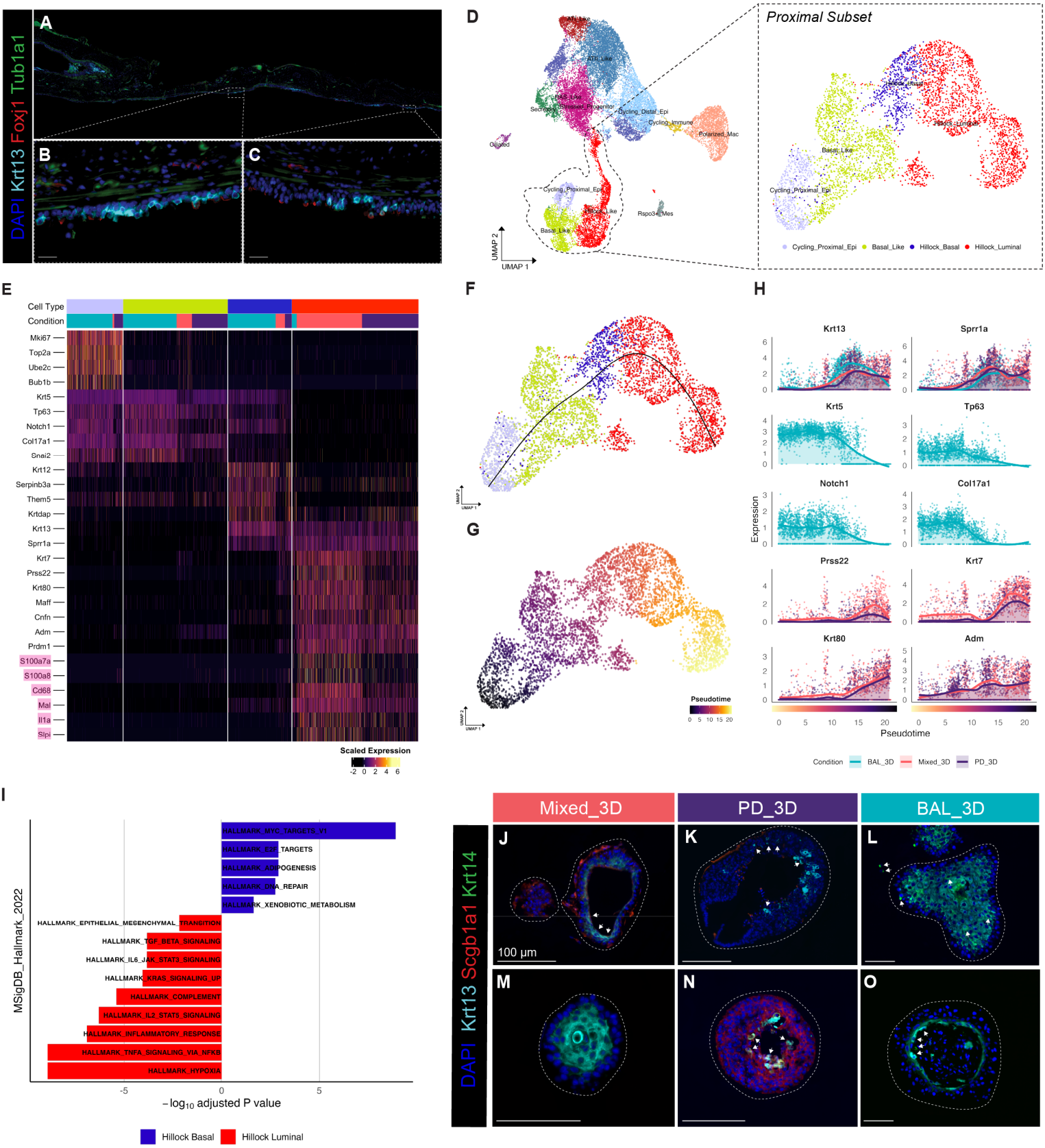

Figure 3. Hillock cells represent a polarized epithelial state with distinct differentiation trajectories and immune-regulatory features. **A–C)** Immunofluorescence staining of native rat trachea reveals clusters of Krt13+ squamous cells (cyan) with Tuba1a (green) and Foxj1ciliated cells (red). These stratified structures resemble hillock domains described in mouse and human airways. Scale bars, 50 µm. **D)** UMAP of the integrated Day 10 single-cell dataset, combining all organoid sequencing data. The right panel shows the subsetted proximal epithelial population, used for downstream trajectory inference and marker analysis. Hillock cells are subdivided into Hillock_Basal (Krt13+/Krt5+) and Hillock_Luminal (Krt13+/Krt5-) populations. **E)** Heatmap of marker gene expression across hillock subtypes, including squamous markers (Krt13, Sprr1a), basal markers (Krt5, Krt14), and immune-associated genes highlighted in pink. **F–G)** Slingshot pseudotime analysis of the proximal epithelial subset reveals a trajectory from cycling progenitors through Basal_Like, Hillock_Basal, and ultimately to Hillock_Luminal cells. **H)** Gene expression trends across pseudotime show stepwise activation of differentiation and immune programs. I) MSigDB Hallmark enrichment analysis comparing Hillock_Luminal and Hillock_Basal populations. **J–O)** Immunofluorescence staining of day 10 organoids shows condition-specific spatial organization of hillock cells. In Mixed_3D **(J, M)** and PD_3D **(K, N)**, Krt13+/Krt14- luminal cells form flattened, apical epithelial layers. In BAL_3D (**L, O**), Krt13+/Krt14+ basal-like cells assemble into multilayered squamous structures (white arrowheads). A subset of hillock luminal cells co-express Scgb1a1 (white arrowheads), supporting a luminal hillock identity. Scale bars, 100 µm.

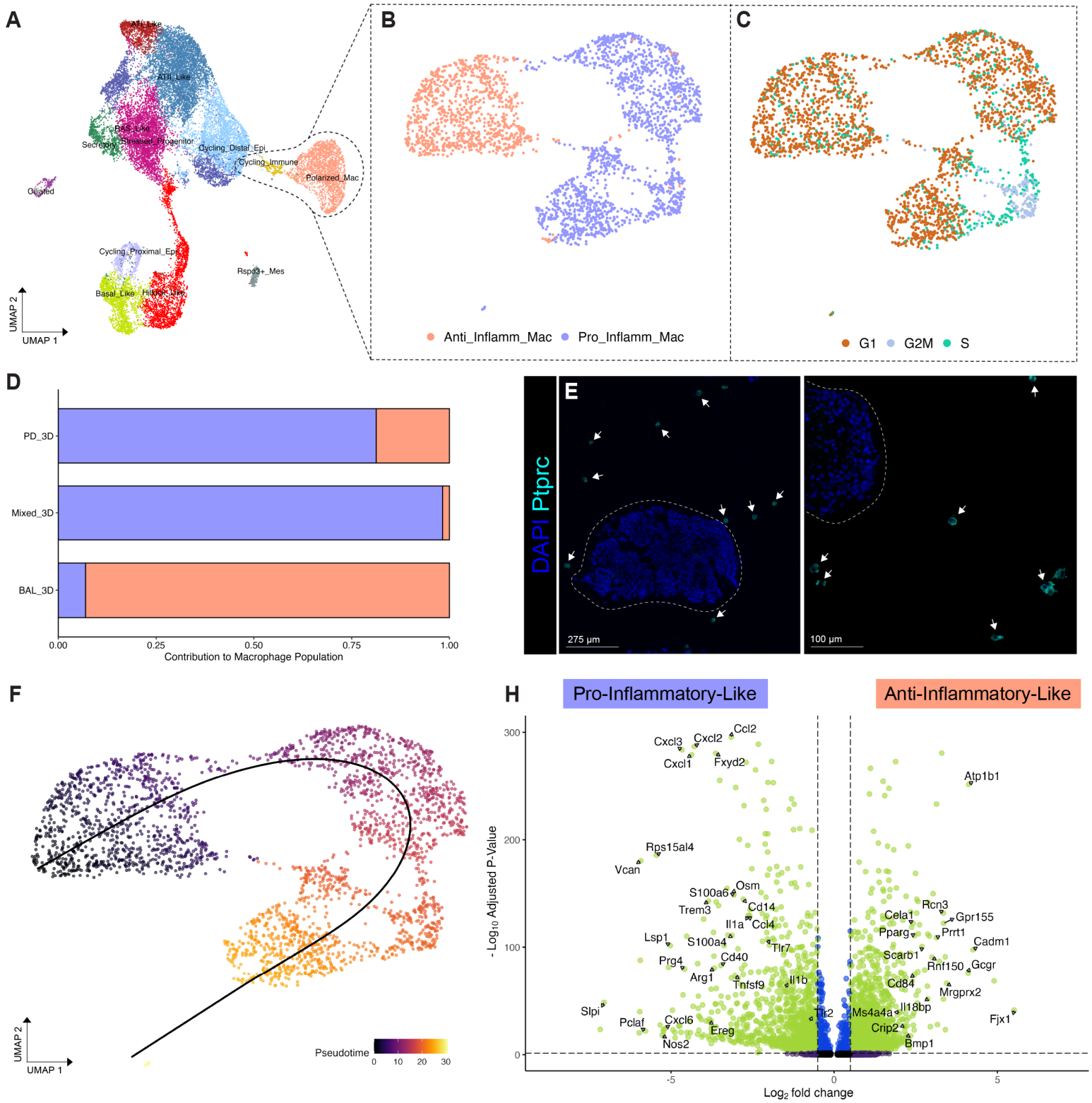

Figure 4. Macrophage polarization trajectories reveal condition-specific immune modulation. **(A)** UMAP of the integrated day 10 organoid dataset highlighting macrophage populations, which cluster as a transcriptionally distinct immune compartment within the broader dataset. **(B)** UMAP of macrophage subset, annotated into two transcriptionally distinct states: anti-inflammatory–like (salmon) and pro-inflammatory–like (lavender). **(C)** Cell cycle phase scoring of macrophages reveals that while most cells are in G1, a subset of pro-inflammatory–like macrophages are cycling, with enrichment in S and G2/M phases. **(D)** Stacked bar plot showing condition-specific contributions to the macrophage population. BAL_3D cultures are enriched for anti-inflammatory–like macrophages, whereas PD_3D and Mixed_3D conditions contain a higher proportion of pro-inflammatory-like macrophages. **(E)** Immunofluorescence staining of day 10 BAL_3D cultures show Ptprc+ alveolar macrophages (cyan) dispersed in the surrounding matrix, often adjacent to but spatially distinct from epithelial organoids (outlined by dashed lines). **(F)** Pseudotime trajectory inferred using Slingshot reveals a transcriptional continuum from anti-inflammatory–like to pro-inflammatory–like macrophage states. **(H)** Volcano plot showing differentially expressed genes between pro- and anti-inflammatory–like macrophages. Pro-inflammatory-like macrophages express elevated levels of inflammatory and alarmin genes (e.g., Cxcl2, Trem1, Il1a, S100a8), while anti-inflammatory-like macrophages upregulate genes associated with tissue remodeling and resolution (e.g., Pparg, Ms4a4a, Cela1).

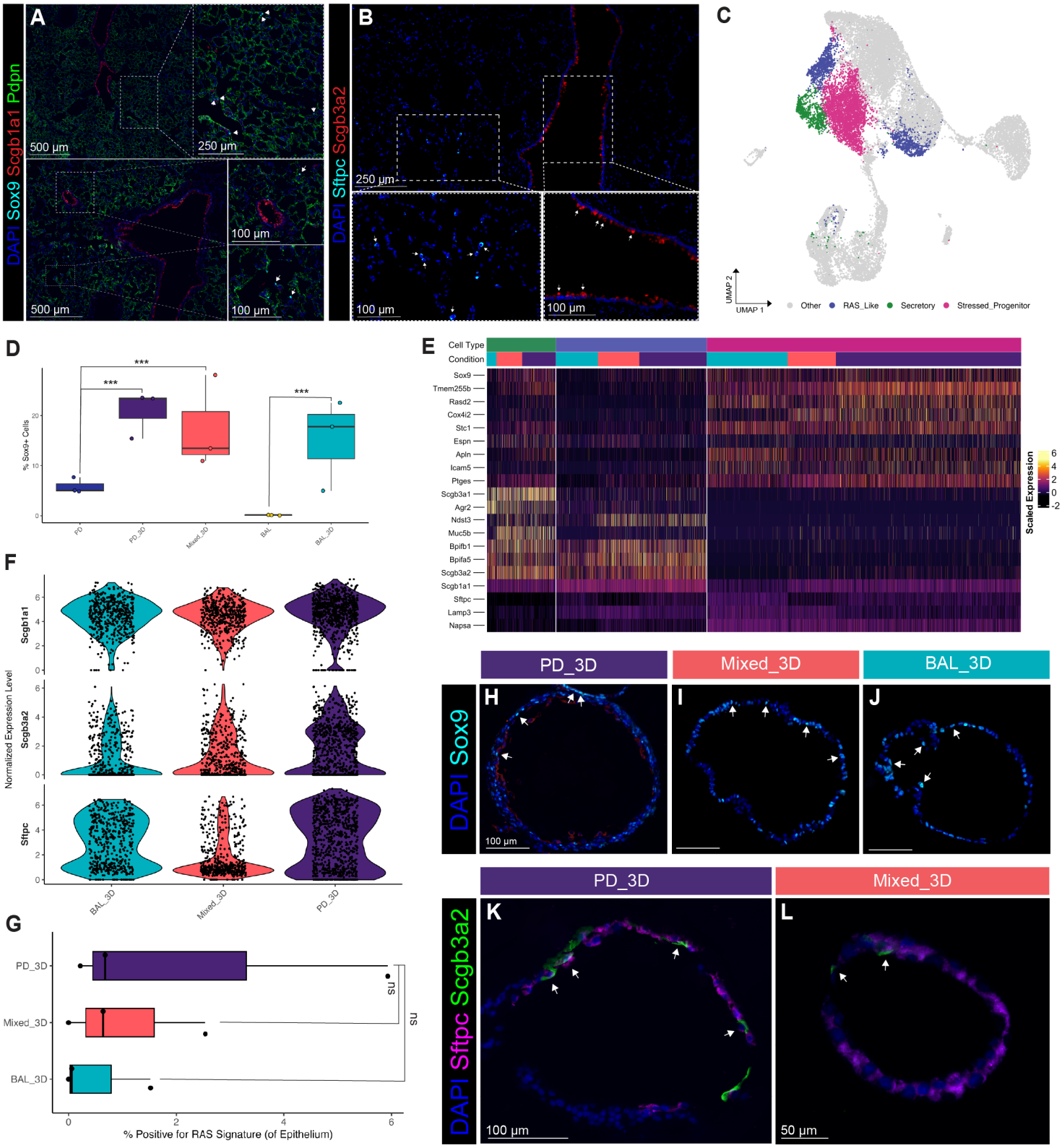

Figure 5. Mesenchyme-rich conditions enrich for secretory-alveolar intermediates, while Sox9+ stressed progenitors emerge across all engineered systems. **(A–B)** Immunofluorescence staining of native adult rat lung reveals rare epithelial progenitor and secretory populations. **(A)** Sox9+ cells (cyan) are observed near the bronchoalveolar duct junction (BADJ), occasionally co-expressing Scgb1a1 (red). Pdpn (green) marks alveolar type I (ATI) cells. **(B)** Scgb3a2+ secretory cells are localized to the conducting airways. Arrowheads highlight individual positive cells. **(C)** UMAP of the integrated day 10 organoid dataset highlights transcriptionally distinct transitional populations, including aRAS/AT0-like, stressed progenitor (Sox9+), and canonical secretory subsets. **(D)** Boxplot quantifying the percentage of Sox9+ cells (threshold: Sox9 expression > 0.1) across five conditions (PD, BAL, PD_3D, Mixed_3D, BAL_3D). Sox9+ cells are rare in the starting populations but expand markedly after 10 days of culture in all conditions. Each point represents an individual biological replicate. Statistical comparisons were performed using two-proportion Z-tests on raw Sox9+ counts, corrected using the Benjamini–Hochberg method (***$p < 0.001$). **(E)** Scaled heatmap showing differential gene expression across transitional epithelial subtypes. aRAS/AT0-like cells (Scgb3a2+/Scgb1a1+/Sftpc+) are distinct from stressed progenitors, which express stress-associated markers (Cox4i2, Ptges, Stc1) alongside the progenitor marker Sox9. **(F)** Violin plots showing expression of signature markers distinguishing canonical secretory and activated RAS-like epithelial populations, split by condition. **(G)** Boxplot showing the percentage of epithelial cells per replicate positive for a RAS-like signature (Scgb1a1+/Scgb3a2+/Sftpc+) across engineered conditions. Signature positivity was determined using scaled expression thresholds: Scgb1a1 > 2, Scgb3a2 > –2.5, and Sftpc > –1.5. Triple-positive cells were observed across all conditions. Statistical comparison using a Kruskal–Wallis test revealed no significant differences in overall frequency; however, the PD_3D group exhibited greater inter-replicate variability, as reflected by its wider interquartile range. **(H–J)** Immunofluorescence staining of day 10 organoids reveal Sox9+ epithelial cells (cyan) variably distributed across all conditions. Scale bars: 100 µm. **(K–L)** Immunofluorescence staining of day 10 organoids (PD_3D and Mixed_3D) showing co-expression of Scgb3a2 (green) and Sftpc (magenta) (RAS-like cells). Scale bars: 100 µm (K), 50 µm (L).

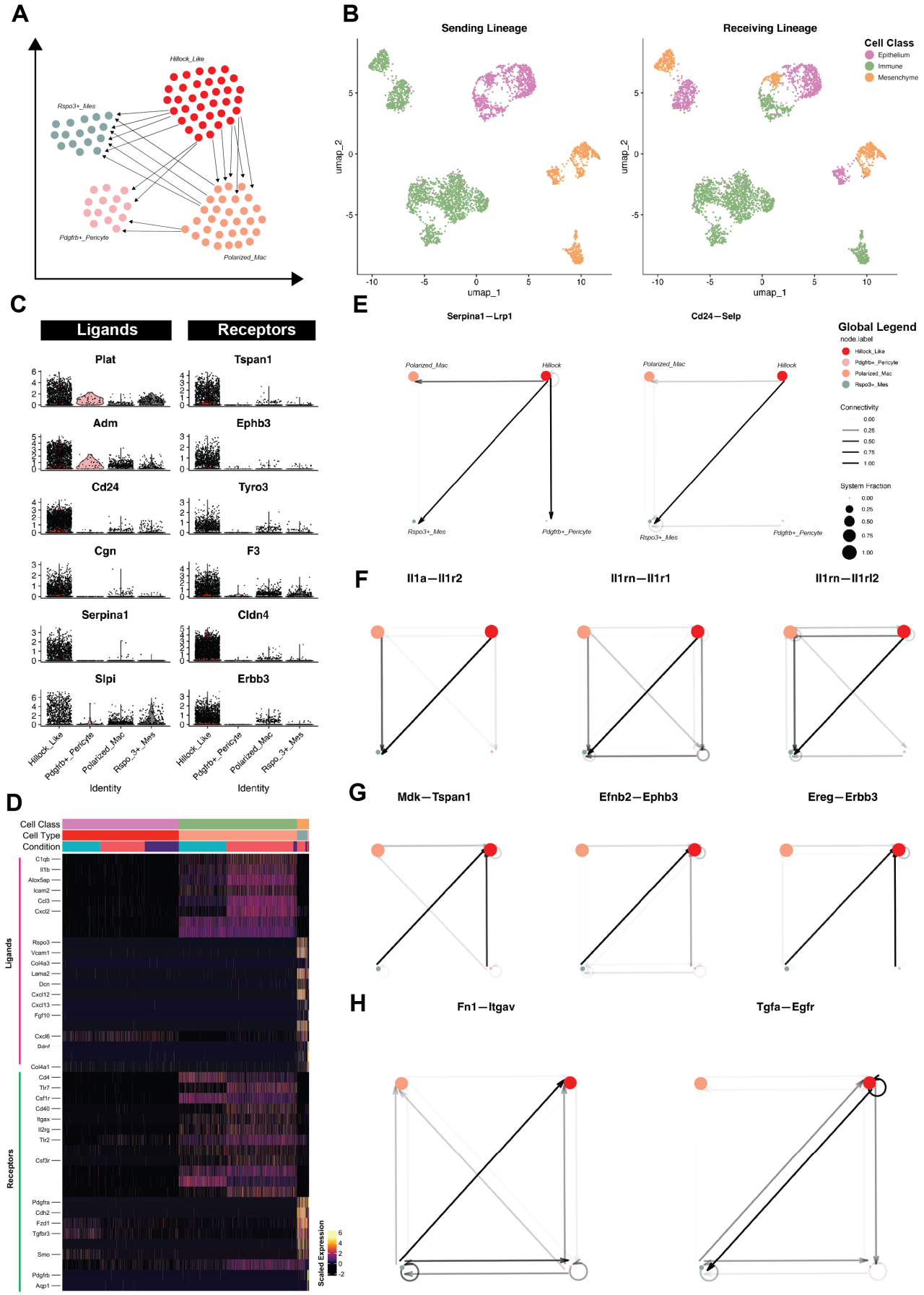

Figure 6. Hillock cells participate in reciprocal signaling circuits that coordinate mesenchymal and immune inputs. **A)** Schematic summary of ligand–receptor interactions between cell populations of interest, inferred using NICHES. Arrows represent directional communication among Polarized_Mac, Pdgfrb+_Pericyte, Rspo3+_Mes, and Hillock_Like epithelial cells. Hillock cells act as central integrators in these networks—orchestrating and responding to diverse mesenchymal and immune-derived signals. **B)** UMAPs showing sending (left) and receiving (right) lineages used for analysis of cell-cell connectivity (NICHES output). **C)** Violin plots showing expression of candidate ligands and receptors enriched in hillock cells. **D)** Scaled heatmap of ligand and receptor expression across cell types and conditions, highlighting transcriptional diversity in connectomic inputs. **E–H)** Circuit plots illustrating inferred cell–cell signaling across selected ligand–receptor axes. Each plot shows directional connectivity betwen sending and receiving populations based on NICHES scoring. Line thickness represents scaled communication strength; node size reflects the relative abundance of each cell population. **E)** Circuits for Serpina1–Lrp1 and Cd24–Selp axes. **F)** Circuits for Il1a–Il1r2, Il1rn–Il1r1, and Il1rn–Il1r2, highlighting inflammatory and regulatory signaling pathways. **G)** Circuits for developmental remodeling signals including Mdk–Tspan1, Efnb2–Ephb3, and Ereg–Erbb3. **H)** Circuits for matrix-associated and EGFR signaling including Fn1–Itgav and Tgfa–Egfr.

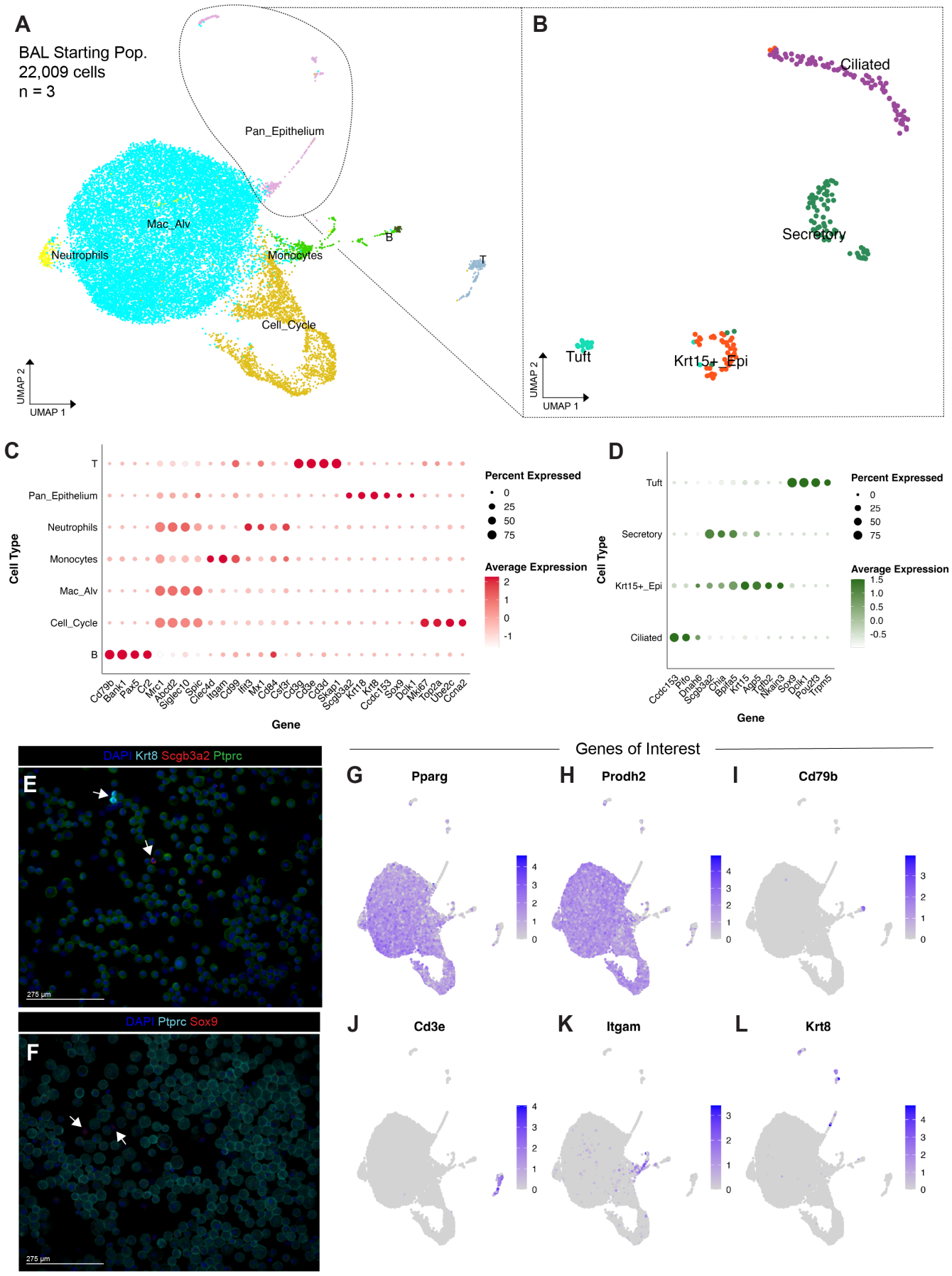

Supplemental Figure 1. Characterization of the BAL starting population prior to 3D culture. **(A)** UMAP visualization of 22,009 single cells derived from bronchoalveolar lavage (BAL) across three biological replicates, identifying major populations including Pan_Epithelium, Macrophages (Mac_Alv), Monocytes, Neutrophils, B cells, and proliferative (Cell_Cycle) cells. **(B)** Sub-clustering of the Pan_Epithelium population from (A) reveals distinct epithelial subsets, including Ciliated, Secretory, Krt15+_Epi, and Tuft cells. **(C–D)** Dot plots displaying expression of canonical marker genes across major cell types **(C)** and epithelial subclusters **(D)**. Dot size reflects the percentage of cells expressing the gene; color indicates scaled average expression. **(E–F)** Immunofluorescence validation of epithelial and immune cell markers in BAL starting population. **(E)** Co-staining for Krt8 (cyan), Scgb3a2 (red), and Ptprc (green) confirms the presence of both epithelial and immune cells; **(F)** Ptprc (cyan) and Sox9 (red) highlight rare Sox9+ cells within the population. Arrows highlight rare epithelial cells. DAPI (blue) marks nuclei. Scale bars = 275 µm.

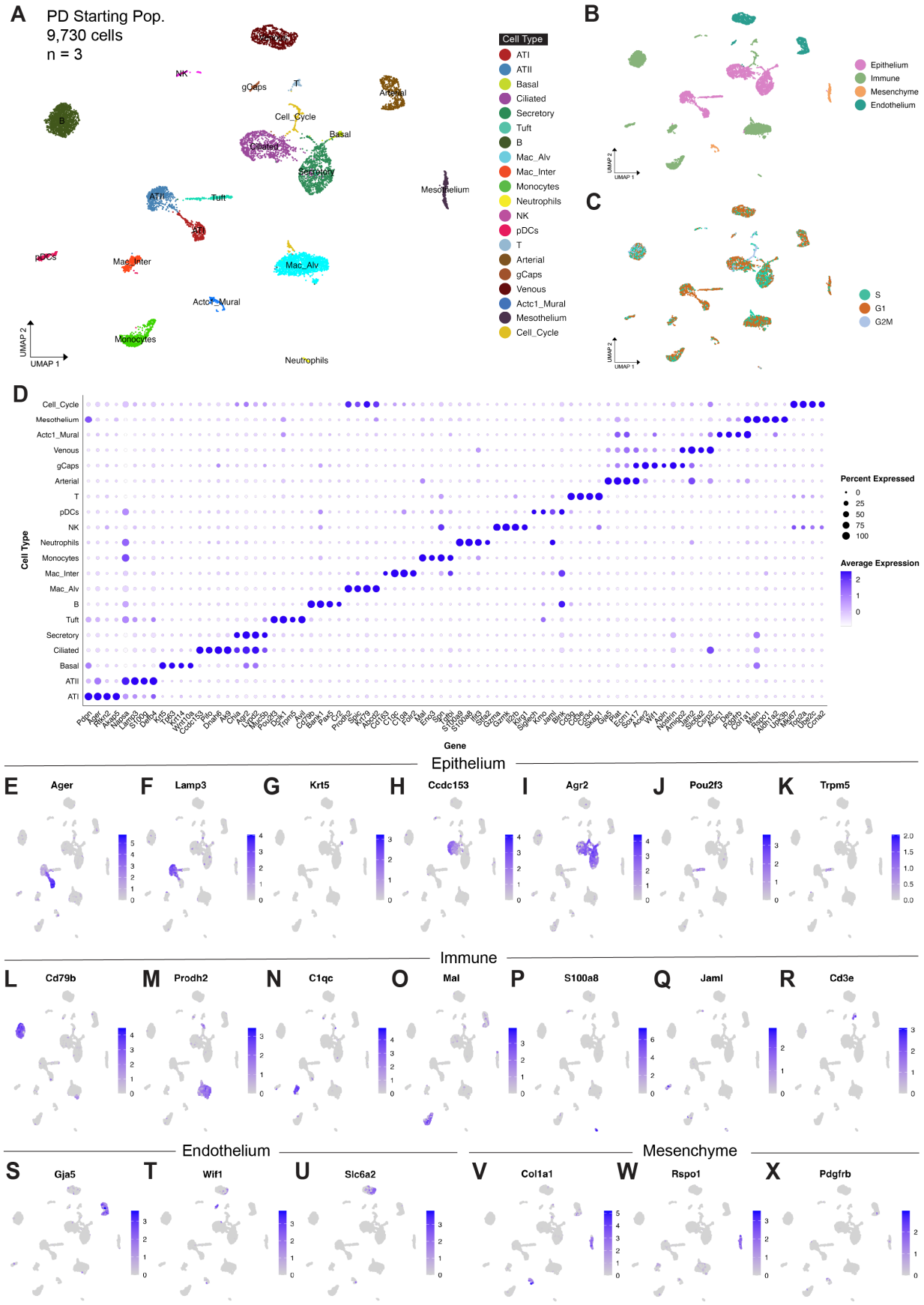

Supplemental Figure 2. Single-cell characterization of the PD starting population prior to 3D culture. **(A)** UMAP embedding of 9,730 single cells derived from the pulmonary dissociation (PD) starting condition across three biological replicates, colored by cell type annotation. Cell populations include epithelial (ATI, ATII, Basal, Secretory, Ciliated, Tuft), immune (Macrophages, Monocytes, Neutrophils, NK, pDCs, B, T), mesenchymal (Actc1_Mural, Mesothelium), endothelial (gCaps, aCaps, Arterial, Venous), and proliferating (Cell_Cycle) cells. **(B)** UMAP colored by broad cell class: Epithelium, Immune, Endothelium, and Mesenchyme. **(C)** UMAP showing cell cycle phase assignment (G1, S, G2M). **(D)** Dot plot displaying expression of canonical markers across annotated cell types. Dot size indicates the percentage of cells expressing each gene, and color intensity represents average expression. **(E–K)** Feature plots showing expression of representative epithelial markers. **(L–R)** Feature plots for immune-related genes of interest. **(S–U)** Feature plots showing endothelial marker markers of interest. **(V–X)** Feature plots showing mesenchymal markers that are representative of the population including Col1a1, Rspo1, and Pdgfrb.

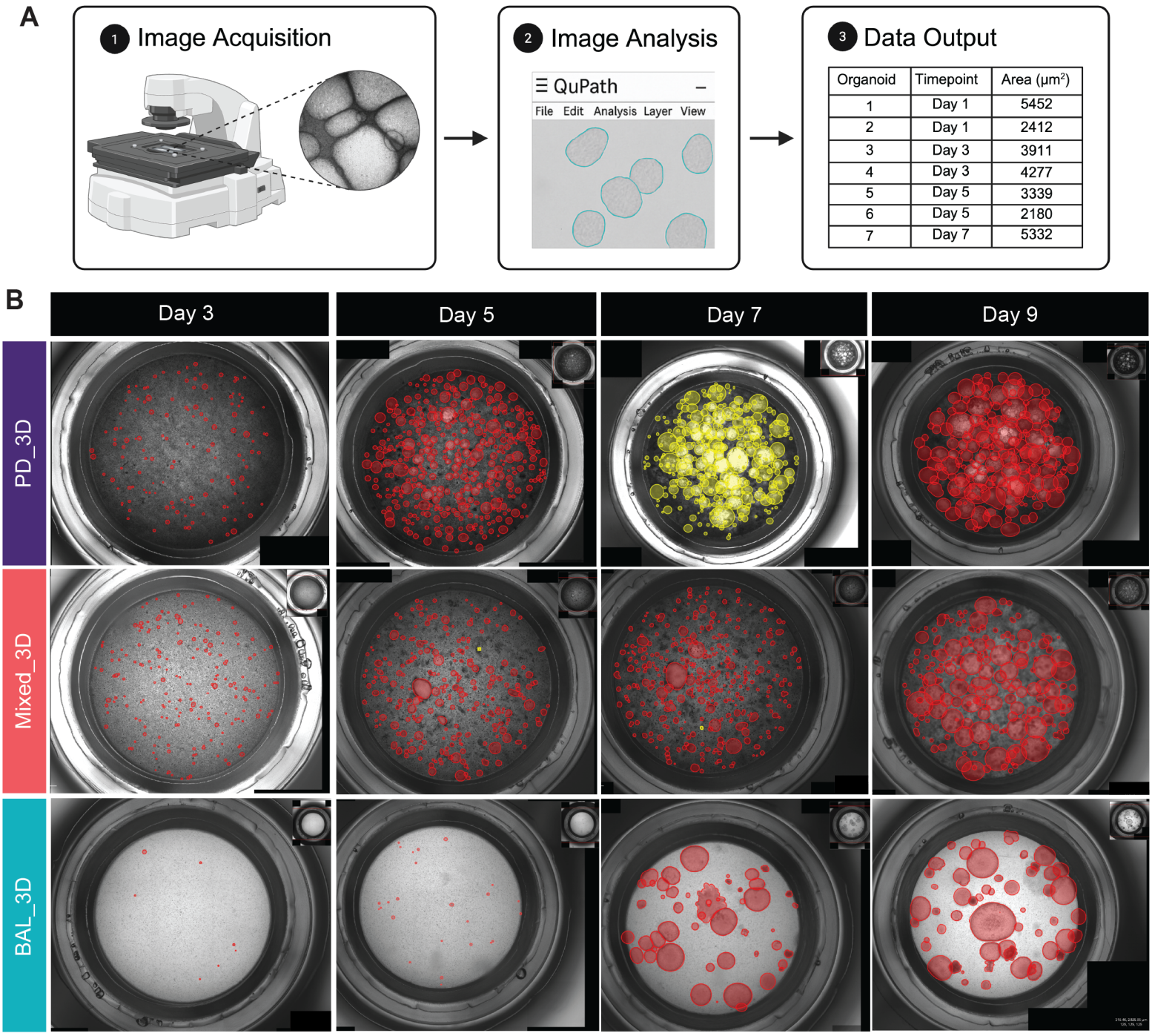

Supplemental Figure 3. Organoid size quantification using QuPath. **(A)** Schematic overview of the image analysis workflow. Brightfield images were acquired at multiple timepoints (Days 0, 3, 5, 7, and 9) using the EVOS FL Auto 2 microscope (4x objective). Stitched images were imported into QuPath (v0.5.1), where organoid boundaries were annotated using the ellipse and brush tools. Organoid area was calculated using a calibrated scale of 1.63 µm/pixel based on the embedded 1 mm scale bar. Quantified area measurements (µm²) were exported for downstream statistical analysis. **(B)** Representative stitched images of entire wells across three culture conditions—PD_3D, Mixed_3D, and BAL_3D—at Days 3, 5, 7, and 9. Red (and yellow, Day 7) overlays indicate detected organoids and their measured boundaries. Variability in organoid number and size is evident across both conditions and timepoints.

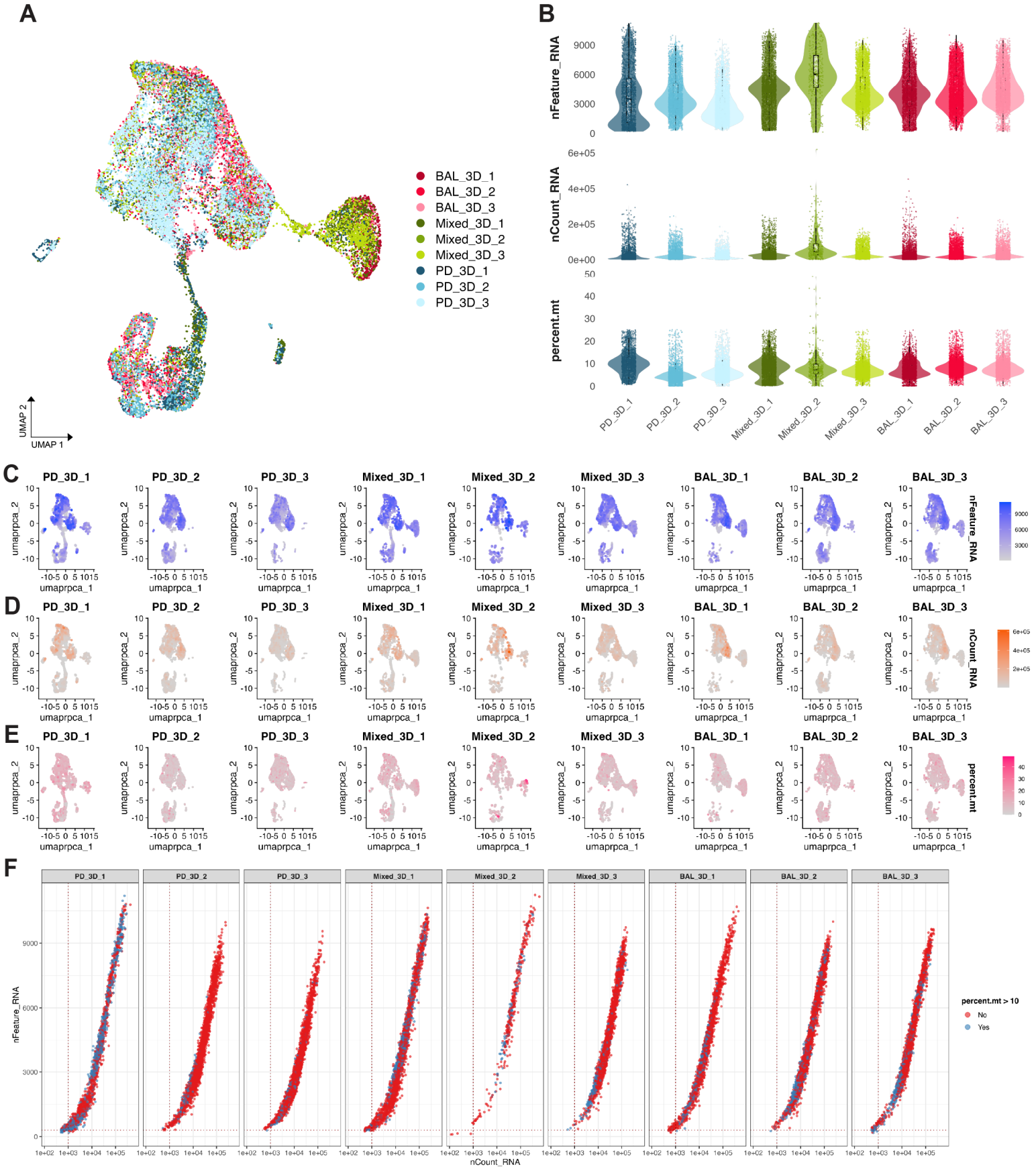

Supplemental Figure 4. Quality control and sample overview of engineered organoid dataset. **(A)** Integrated UMAP embedding of all engineered samples grouped and colored by experimental replicate (Orig_ID). Samples include BAL-derived (BAL_3D_1–3), Mixed (Mixed_3D_1–3), and PD-derived (PD_3D_1–3) organoids. **(B)** Violin plots showing the distributions of raw (untransformed) values by sample (replicate): number of genes detected per cell (nFeature_RNA), total RNA counts (nCount_RNA), and percentage of mitochondrial transcripts (percent.mt). Boxplots indicate interquartile range and median; individual cells are overlaid as jittered points. **(C–E)** Split UMAP feature plots for each sample showing expression of nFeature_RNA **(C)**, nCount_RNA **(D)**, and percent.mt **(E)**. **(F)** Scatter plots showing nCount_RNA (log10 scale) versus nFeature_RNA (linear scale) for individual cells, faceted by sample (Orig_ID). Cells are colored by mitochondrial transcript abundance, with blue indicating cells exceeding 10% mitochondrial RNA (percent.mt > 10). Red dotted lines indicate commonly used quality control thresholds (nFeature_RNA = 300, nCount_RNA = 1,000).

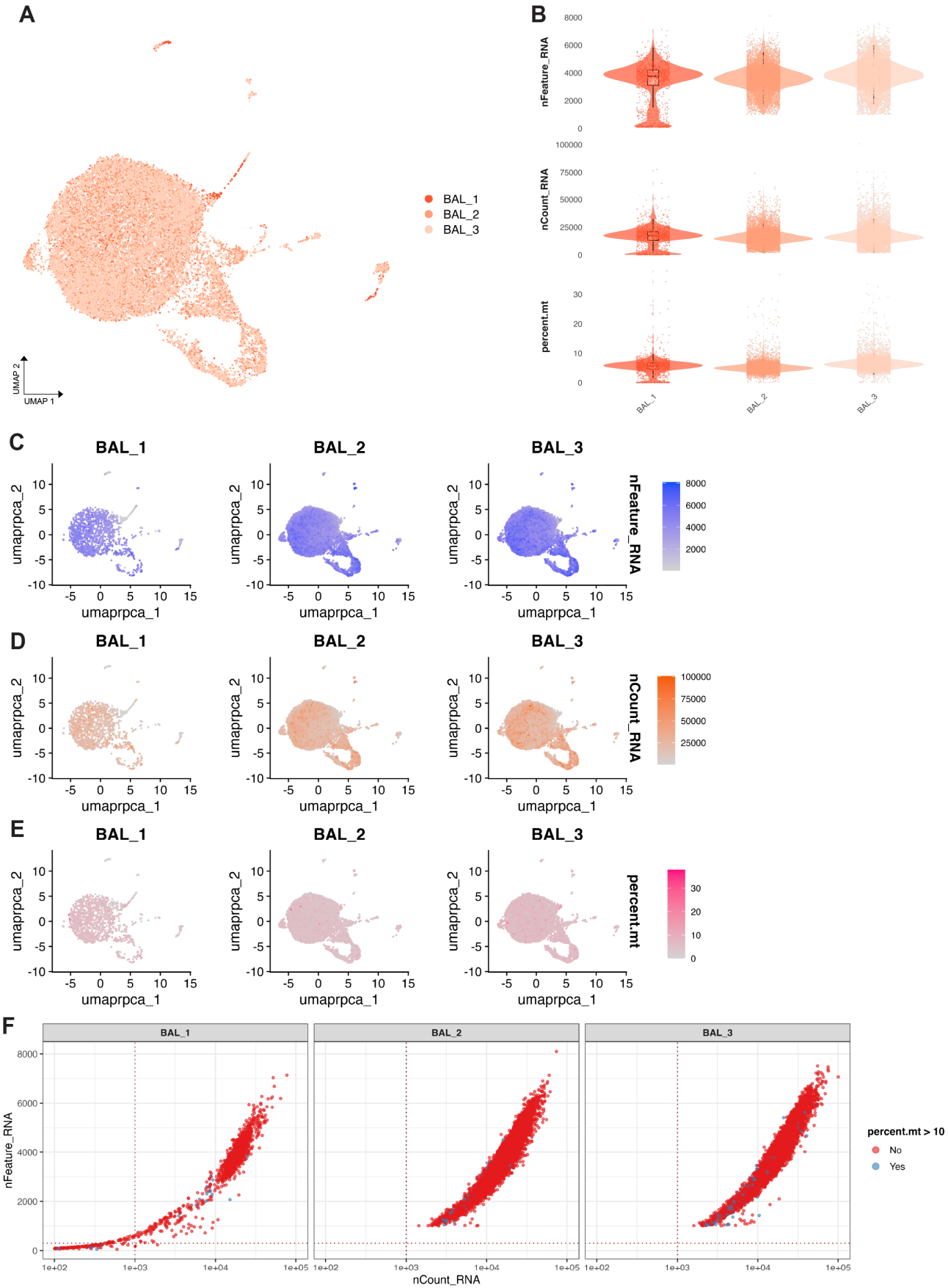

Supplemental Figure 5. Quality control and sample overview of BAL starting population. **(A)** Integrated UMAP embedding of all BAL starting cells grouped and colored by experimental replicate (Orig_ID; BAL_1–3). **(B)** Violin plots showing the distributions of raw (untransformed) quality control metrics across replicates: number of genes detected per cell (nFeature_RNA), total RNA counts (nCount_RNA), and percentage of mitochondrial transcripts (percent.mt). Boxplots indicate interquartile range and median; individual cells are overlaid as jittered points. **(C–E)** Split UMAP feature plots for each replicate showing expression of nFeature_RNA **(C)**, nCount_RNA **(D)**, and percent.mt **(E)**. **(F)** Scatter plots showing nCount_RNA (log10 scale) versus nFeature_RNA (linear scale) for individual cells, faceted by replicate. Cells are colored by mitochondrial transcript abundance, with blue indicating cells exceeding 10% mitochondrial RNA (percent.mt > 10). Red dotted lines indicate quality control thresholds used for filtering (nFeature_RNA = 300, nCount_RNA = 1,000, percent.mt = 10%).

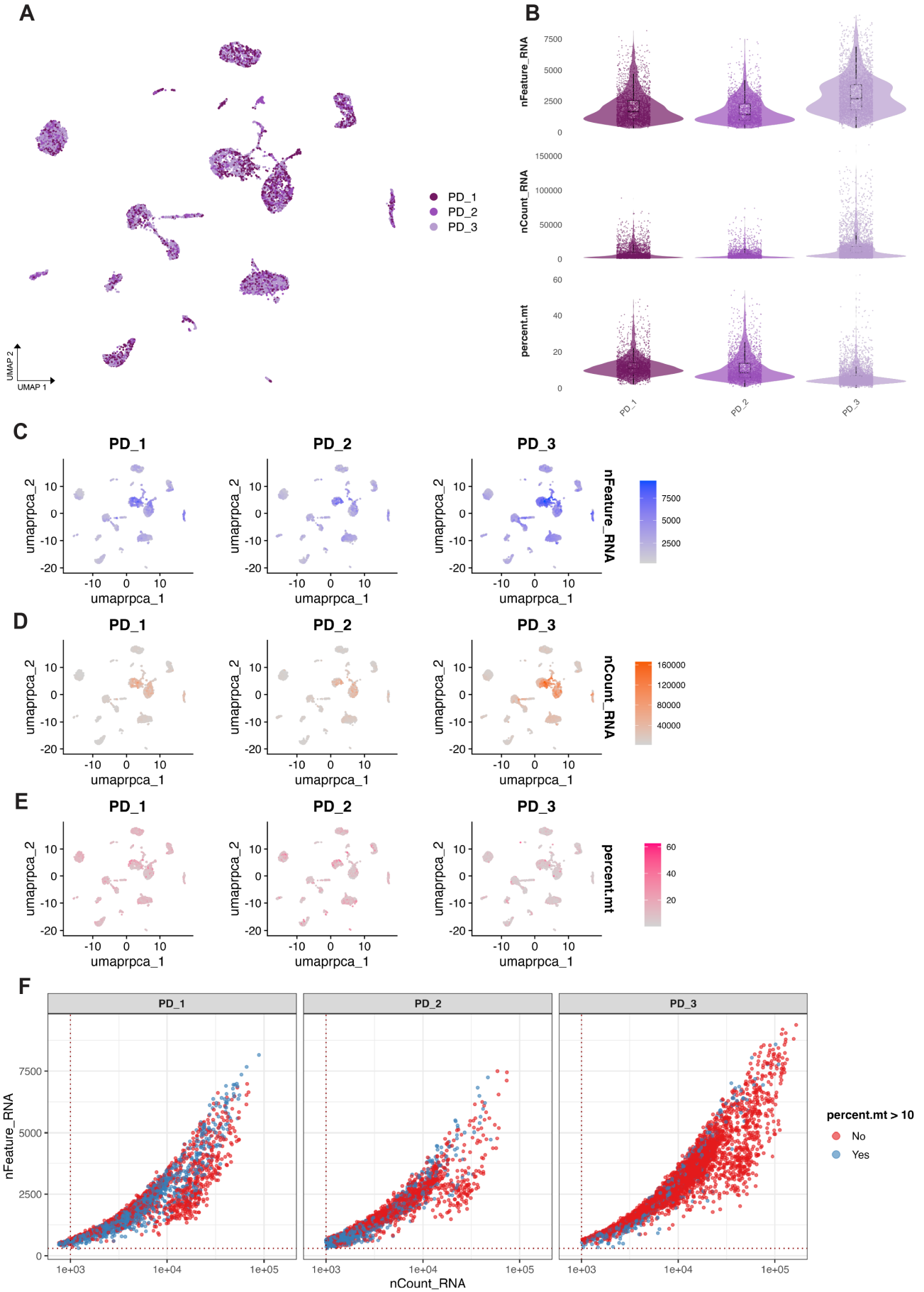

Supplemental Figure 6. Quality control and sample overview of PD starting population. **(A)** UMAP embedding of all pulmonary dissociation (PD) starting cells, grouped and colored by experimental replicate (Orig_ID; PD_1–3). **(B)** Violin plots showing the distributions of raw (untransformed) quality control metrics across replicates: number of genes detected per cell (nFeature_RNA), total RNA counts (nCount_RNA), and percentage of mitochondrial transcripts (percent.mt). Boxplots indicate interquartile range and median; individual cells are overlaid as jittered points. **(C–E)** Split UMAP feature plots for each replicate showing expression of nFeature_RNA **(C)**, nCount_RNA **(D)**, and percent.mt **(E)**. **(F)** Scatter plots showing nCount_RNA (log10 scale) versus nFeature_RNA (linear scale) for individual cells, faceted by replicate (PD_1–3). Cells are colored by mitochondrial transcript abundance, with blue indicating cells exceeding 10% mitochondrial RNA (percent.mt > 10). Red dotted lines indicate commonly used quality control thresholds (nFeature_RNA = 300, nCount_RNA = 1,000).

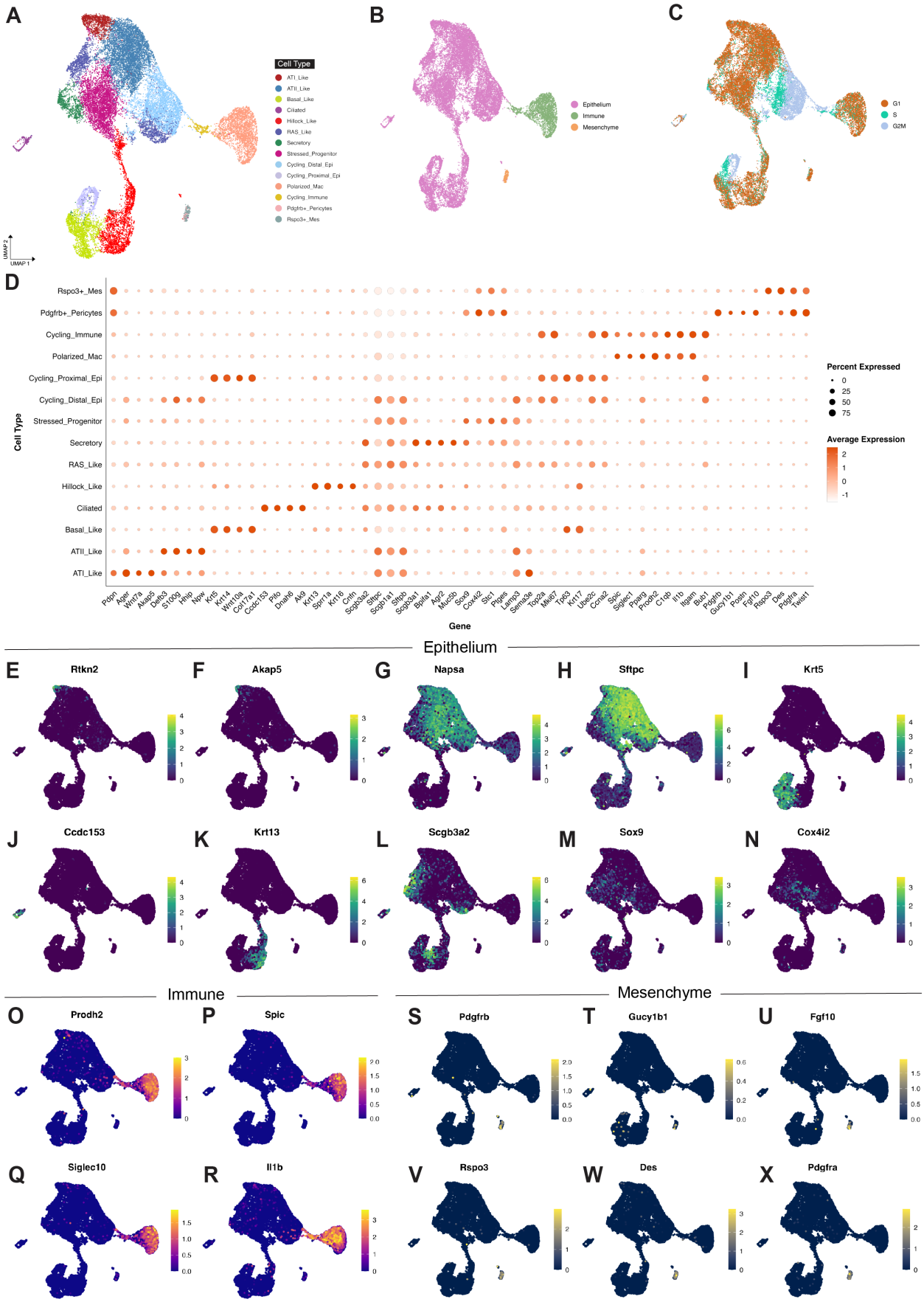

Supplemental Figure 7. Marker-based cell type annotation in engineered organoid single-cell dataset (global object, all three organoid conditions). **(A)** Integrated UMAP embedding of all cells from engineered organoid samples colored by annotated cell type, including epithelial (e.g., ATI_Like, ATII_Like, Secretory, Hillock_Like, RAS_Like), immune (e.g., Polarized_Mac, Cycling_Immune), and mesenchymal (e.g., Rspo3+_Mes, Pdgfrb+_Pericytes) populations. **(B)** Same UMAP colored by broad cell class: Epithelium, Immune, and Mesenchyme. **(C)** UMAP colored by cell cycle phase assignment (G1, S, G2M). **(D)** Dot plot showing expression of canonical marker genes across annotated cell types for justification. Dot size indicates the proportion of cells expressing the gene; color reflects scaled average expression. **(E–N)** Feature plots showing expression of epithelial markers including Rtkn2 (AT1), Akap5 (AT1), Napsa (AT2), Sftpc (AT2), Krt5 (Basal), Ccdc153 (Ciliated), Krt13 (Hillock), Scgb3a2 (Secretory/RAS), Sox9 (Stressed_Progenitor), and Cox4i2 (Stressed_Progenitor). **(O–R)** Expression of immune-associated genes including Prodh2, Spic, Siglec10, and Il1b. **(S–X)** Feature plots of mesenchymal markers such as Pdgfrb (pericyte), Gucy1b1 (pericyte), Fgf10, Rspo3, Des, and Pdgfra, supporting identification of mesenchymal subpopulations.

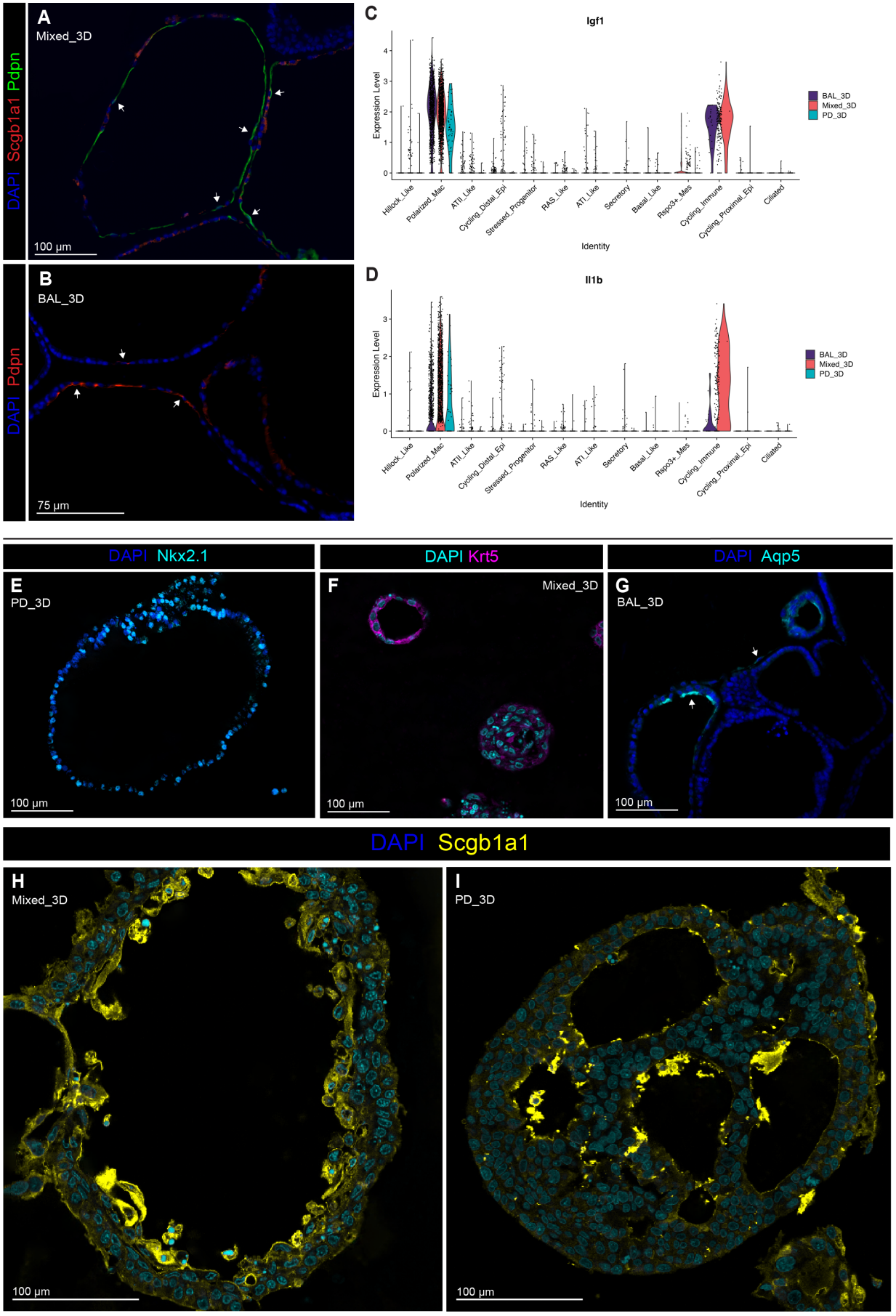

Supplemental Figure 8. Drivers of ATI-like differentiation and additional epithelial immunofluorescence staining across organoid conditions. **(A–B)** Immunofluorescence staining of day 10 organoids reveal spatial separation between Pdpn+ alveolar type I (ATI) cells (green) and Scgb1a1+ secretory cells (red), with arrowheads indicating Pdpn+ segments along the epithelial border in **(A)** Mixed_3D and **(B)** BAL_3D cultures. **(C–D)** Violin plots showing expression of Igf1 and Il1b across immune populations. Igf1 expression is highest in the BAL_3D condition. **(E–G)** Immunofluorescence staining of day 10 organoids for additional epithelial lineage markers: **(E)** Nkx2.1 (cyan) marks ATII-like cells; **(F)** Krt5 (magenta) labels basal-like cells; **(G)** Aqp5 (cyan) marks ATI-like cells, with arrows highlighting localized expression along squamous regions of the epithelial border. **(H–I)** Immunofluorescence staining for Scgb1a1 (yellow) in **(H)** Mixed_3D and **(I)** PD_3D conditions shows variable distribution of secretory epithelial cells across organoid structures.

Supplemental Table S1. LPM-3D Growth Medium Components (adapted from Nichane et al., 2017)

Classifier	Component	Concentration	Supplier	Ref. #
Basal Medium	Advanced DMEM/F12	N/A	ThermoFisher	12634010
Growth Factor (GF)	FGF10	50 ng/mL	Peprotech	400-42
GF	FGF9	50 ng/mL	Novus Biologics	NBP-35196
GF	EGF	50 ng/mL	Peprotech	400-25
Small Molecule (SM)	CHIR99021 (GSK-3 Inhibitor)	3 μM	Cayman Chemicals	13122-10
SM	BIRB796	1 μM	Cayman Chemicals	10460-10
SM	Y27632 (Rock Inhibitor)	10 μM	Cayman Chemicals	10005583-10
SM	A8301 (ALK-5/TGF-beta/NODAL Inhibitor)	1 uM	Cayman Chemicals	9001799-10
Additional Components (AC)	Heparin	5 μg/mL	Sigma-Aldrich	H3149-10KU
AC	Insulin	10 μg/mL	Sigma-Aldrich	910077C-100
AC	Transferrin	15 μg/mL	Sigma-Aldrich	T8158-100
Antibiotics (AB)	PenStrep	1x	ThermoFisher	15140122
AB	Glutamine	1x	ThermoFisher	25030081
AB	Anti-Anti	0.25 mg/L	ThermoFisher	15240062
AB	G418	50 μg/mL	ThermoFisher	10131035

Supplemental Table S2. Primary Antibodies with Dilutions Used for Immunohistochemistry

Antibody	Supplier	Product #/ Identifier	Cell Type	Dilution
Goat anti-Foxj1	Santa Cruz Biotechnology, Inc.	sc-54371	Ciliated epithelium (nuclear)	1:100
Rabbit anti-CD45 (Ptprc)	Abcam	ab10558	Pan-immune	1:100
Mouse anti-CD45 (Ptprc)	BD Biosciences	554875	Pan-immune	1:100
Goat anti-CCSP (Uteroglobin / Scgb1a1)	EMD Millipore	ABS1673	Secretory cells	1:100
Goat anti-UGRP1/ SCGB3A2	R&D Systems	AF3545	Secretory cells	1:200
Mouse anti-RTI-40 (Podoplanin)	Terrace Biotech	TB-11ART1-40	Alveolar type II cells (rat specific)	1:40
Mouse anti-Acetylated Tubulin	Sigma	T7451	Epithelium; cilia specific.	1:200
Rabbit anti-Krt13	Abcam	ab92551	Hillock cells	1:100
Mouse anti-Krt14	Abcam	ab9220	Basal cells	1:100
Rabbit anti-proSPC	Millipore	AB3786	ATII cells	1:100
Rabbit anti-Sox9	Abcam	ab185966	BASCs	1:100
Rabbit anti-Krt8	Abcam	ab59400	Transitional epithelium	1:100

Supplemental Table S3. Secondary Antibodies with Dilutions Used for Immunohistochemistry

Antibody	Supplier	Product #/ Identifier	Species	Dilution
Donkey anti-Rabbit IgG (H+L) Alexa Fluor 647	Invitrogen	A31573	Donkey	1:500
Donkey Anti-Goat IgG (H+L), Alexa Fluor 555	Invitrogen	A21432	Donkey	1:500
Donkey Anti-Mouse IgG (H&L), DyLight 488	Abcam	ab96875	Donkey	1:500
Donkey Anti-Mouse IgG (H+L), Alexa Fluor 488	Invitrogen	A21202	Donkey	1:500

Supplemental Table 4 (S4): Initial cutoffs and final clustering resolutions used for each individual scRNAseq sample

Sample ID	nCount_RNA Initial Cutoff	Final Embedding Resolution
PD_1	**750**	**0.5**
PD_2	**1000**	**0.2**
PD_3	**1000**	**0.35**
BAL_1	**100**	**0.5**
BAL_2	**1000**	**0.3**
BAL_3	**1000**	**0.3**
PD_3D_1	**500**	**0.5**
PD_3D_2	**500**	**0.8**
PD_3D_3	**500**	**0.45**
Mixed_3D_1	**500**	**0.42**
Mixed_3D_2	**100**	**0.4**
Mixed_3D_3	**100**	**0.5**
BAL_3D_1	**500**	**0.38**
BAL_3D_2	**500**	**0.5**
BAL_3D_3	**500**	**0.5**